MULTIPLE ORIGINS OF SAND-DUNE TOPOGRAPHY INTERACTIONS ON TITAN

A Thesis

by

HOLLY ELAINE GOGGIN

Submitted to the Office of Graduate and Professional Studies of
Texas A&M University
in partial fulfillment of the requirements for the degree of

MASTER OF SCIENCE

Chair of Committee,	Ryan Ewing
Committee Members,	Rick Giardino
	Mark Lemmon
Head of Department,	Mike Pope

December 2016

Major Subject: Geology

ABSTRACT

The interaction between sand-dune patterns and topographic obstacles is a primary signal of sand transport direction in the equatorial region of Saturn's moon, Titan. A streamlined, tear drop appearance emerges as dune crestlines wrap around topographic obstacles and a dune-free zone develops on the east side of many obstacles. The morphologies formed by this interaction give the impression that sand transport is from the west to east in Titan's equatorial region. However, this transport direction is in conflict with the expected wind regime based on Titan's rotation and many global climate models. The physical mechanism behind the interpretation of the dune-obstacle interaction is not well explained, leaving a gap in the understanding of the sand transport and equatorial wind directions on Titan. In order to better understand this interaction and evaluate wind and sand transport direction on Titan, we take a two-fold approach to studying dune-topography interactions. We use optical imagery on Earth and Cassini radar imagery on Titan in ArcGIS to map spatial variations in dune crestline orientations proximal to obstacles. We also use digital elevation models to analyze the three-dimensional geometry – height, length, width and slope of the dune-topography relationships on Earth. We identify three types of obstacles: positive topography, neutral topography and negative topography. Positive topography is defined as double or more in relief than the surrounding dune height, neutral topography is at the surrounding dune height and negative topography is lower than the surrounding dune heights. Results show that dune patterns are deflected further away from positive relief than neutral or

negative relief. Furthermore, positive relief has a dune free obstacle shadow, neutral relief has a smaller dune free obstacle shadow to no obstacle shadow zone, and negative relief has an obstacle shadow zone characterized by increased dune wavelength proximal to the obstacle's wind-shielded side. The obstacle height, width, slope and wind variability appear to play a role in determining if a lee-dune, rather than a dune-free lee-zone forms. These factors provide further geomorphic evidence that sand transport directions on Titan were from west to east during the formation of the dune-obstacle interaction morphologies.

ACKNOWLEDGEMENTS

I would like to thank my committee chair, Dr. Ewing, for his support and invaluable guidance throughout this project. I also wish to thank my committee members Dr. Giardino, and Dr. Lemmon, for their contributions in the form of ideas and discussions. Additional thanks goes to Dr. Swann, Dr. Epps, and Mrs. Breed for their helpful advice and contributions to this project.

I also want to extend my gratitude to NASA Cassini Data Analysis, which provided a grant to support this work, the Marathon Oil for their support via a Diversity Scholarship, and the Texas A&M University Department of Geology and Geophysics for their funding via a teaching assistantship.

Finally, thanks to my mother, father, and sister for their encouragement.

TABLE OF CONTENTS

Page

Page

LIST OF FIGURES

1. INTRODUCTION

Titan, a moon of Saturn, is covered by sand dunes between 30 degrees north and south of the equator (Lorenz et al., 2006; Radebaugh et al., 2008; Elachi et al., 2006, 2010; Mastrogiuseppe et al., 2014). Dunes have a mean crestline length of 50 km, a mean crest spacing between 2 and 3 km, and are oriented 270 degrees azimuth ± 11 degrees (Barnes et al., 2008; Radebaugh et al., 2008; Lorenz and Radebaugh, 2008; McDonald et al., 2016). The dune sand composition is thought to be organic materials such as hydrocarbon dust or nitrile grains, tholins, organic covered ice, or CO2 ice, based on spectral properties and atmospheric organic material production models (Griffith et al., 2003; Soderblom et al., 2007; Janssen et al., 2009; Barnes et al., 2015). These suggested materials are thought to be 300 μm based on wind tunnel modeling (Burr et al., 2015), and may reach the predicted sand size by sintering, lithification, flocculation, or evaporate formation (Barnes et al., 2015). Based on morphology, Titan's dunes are linear and thought to be elongating from west to east based on the interaction of linear pattern with the topographic obstacles within the dune field (Lorenz et al., 2006; Radebaugh et al., 2008; Neish et al., 2010).

The explanation that the dunes are elongating from west to east hinges on the interpretation of the landscape morphology that forms from the interaction of Titan's dunes and isolated topographic obstacles within the dune field. Dunes deflect laterally around obstacles and transition into a streamlined, tear-drop shape on the inferred downwind direction (Figure 1). This streamlined shape of the dune-obstacle interaction

is the primary basis for the west-to-east transport direction. However, this interpretation conflicts with the observed rotation of Titan and the expected easterly winds that arise from the conservation of momentum between the spinning solid surface and the atmosphere. Global Circulation Models (GCMs) and geomorphic studies predict a range of wind conditions that cannot entirely explain the west-to-east elongation (Lebonnois et al., 2012; Lora et al., 2015; Tokano, 2008, 2010). Alternative explanations that offer hypothesis to explain an west-to-east elongation include methane storms (Charnay et al., 2015; Huseo and Sanchez-Lavega, 2006), Intertropical Convergence Zone (ITCZ) winds (Tokano, 2010), and long-term climate cycles (Ewing et al., 2014).

This study examines how topographic obstacle shape modifies dune-field patterns using Earth-analog study sites in comparison to Titan's dune fields. Characteristic pattern parameters such as dune orientation, spacing, and crest length are mapped at 25 sites in five deserts, which contain topographic obstacles within dune fields. The paper first discusses the analog study areas and presents results that show trends in dune reorientation patterns and dune spacing associated with specific regions around an obstacle. The discussion reviews the type and origins of obstacle-modified dunes and discusses the interpretation of sand transport direction, wind direction, and boundary conditions from dune-obstacle interactions on Earth and Titan.

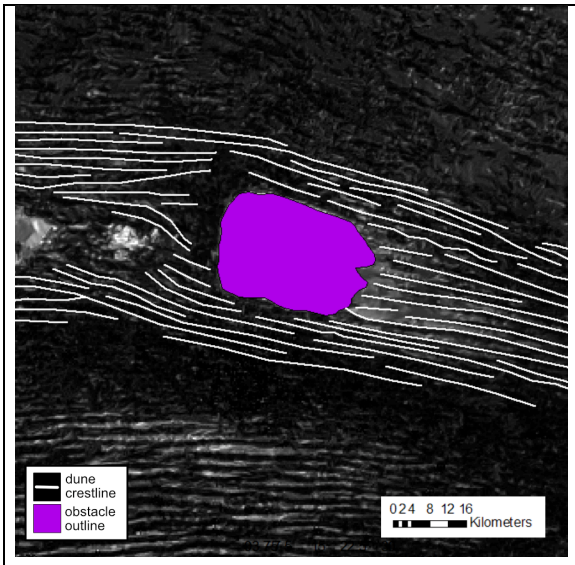

Figure 1a.

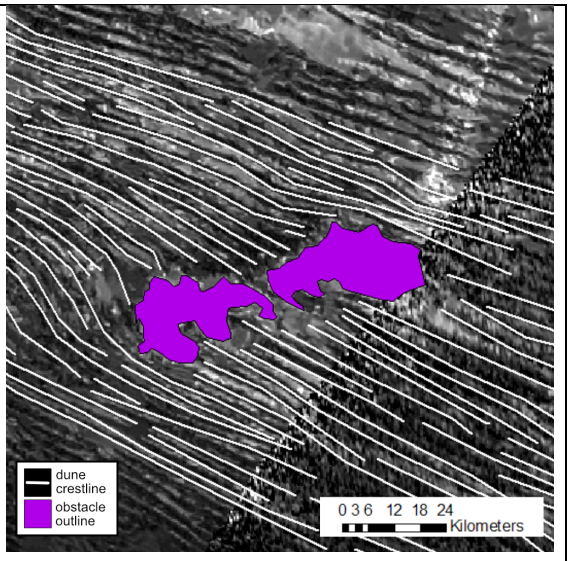

Figure 1b.

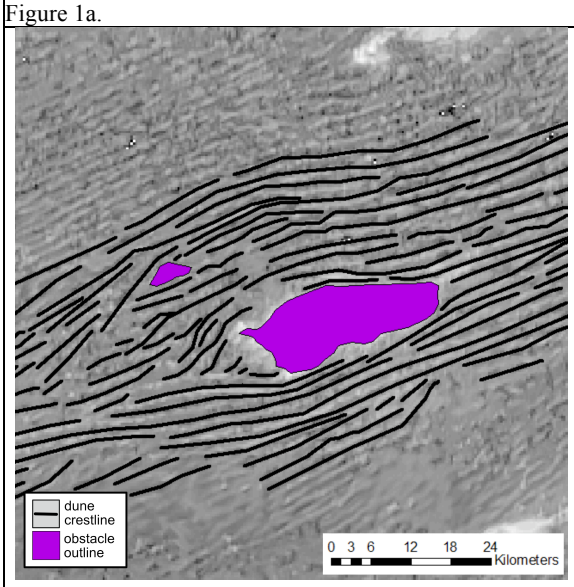

Figure 1c.

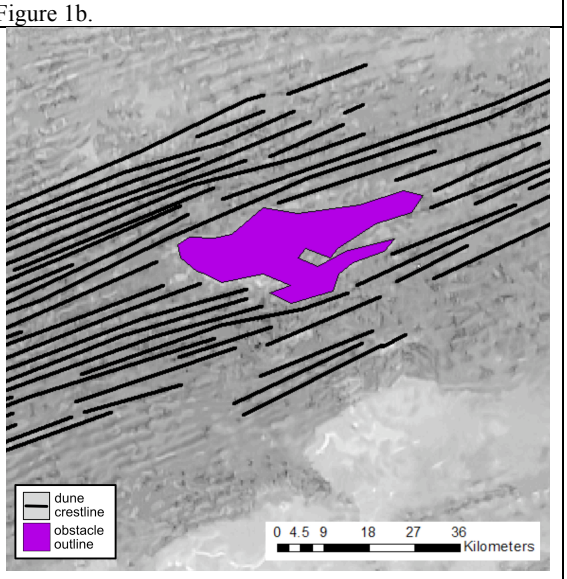

Figure 1d.

Figure 1. Digitally polygoned obstacles from Titan's Fensal (a,b) and Senkyo (c,d) dune fields. The target obstacles are in purple at center. White lines for Fensal and black lines for Senkyo are manually digitized crests. Mapping conducted using a mosaicked Synthetic Aperture Radar (SAR) image. Dunes are interpreted as dark lineations surrounding the bright area at the center of the field (polygoned in purple) interpreted to be a topographic-obstacle. Note the high density of dunes on the west side of the obstacle and mottled area to the east with increased dune spacing

This study examines how topographic obstacle shape and relief modify dune patterns using Earth-analog study sites and comparison to Titan's dune fields. Characteristic pattern parameters such as dune orientation, spacing, and crest length are mapped at 25 sites in five deserts, which contain topographic-obstacles within dune fields. The paper first discusses the analog study areas and presents results that show that trends in dune reorientation patterns and dune spacing changes can be associated with certain regions around an obstacle. The discussion reviews the type and origins of obstacle-modified dunes and discusses the interpretation of sand transport direction, wind direction, and boundary conditions from dune-obstacle interactions on Earth and Titan.

2. STUDY AREAS

Five desert regions on Earth were selected based on the presence of linear, longitudinal dunes and isolated topography that sits within the field of longitudinal dunes. These sites are within the Kalahari Desert, the Namib Desert, the Ramlat Sand Sea and the Irq Al Idrisi Sand Sea in Libya, the Negev and Sinai Desert, and the Western Sahara Desert.

2.1 Namib Desert

The Namib Desert is a 34,000 km^2 dune field (Figure 2a), located in southwest Africa. This desert is characterized by linear, longitudinal dunes in the central and northern portions of the field, with crestlines oriented roughly north to south by the seasonally varying winds from the northeast and southwest (Lancaster, 1981). Barchaniod transverse dunes can also be found in a 20-30 km wide region along the Namib coast (Lancaster, 1981), with the entire dune field thought to have developed in the Pliocene (Miller, 2014). The dunes' sediment source has been primarily attributed to the Orange River (Garzanti, 2012), which delivers sediment to the coast, where the material is mobilized back onshore by ocean currents and subsequently by coastal winds from the beach sands found west of the dune field into the Namib desert (Lancaster, 1981; Stone, 2013). Additional, but less abundant sediment sources include recycled underlying Tsodab sandstone bedrock and more locally along the eastern region of the Namib by the hinterland rivers Kuiseb and Tsonab (Garzanti, 2012; Lancaster, 1981).

Rock outcrops of the Tsondab and Sossus Sandstons Formations (Ward, 1988) are used in this study as topographic obstacles. The Tsonab Sanstone Formation is a unit of aeolian dune, sand sheet, fluvial, and playa deposits, while the Sossus Sandstone Formation is characterized by aeolian deposits (Ward, 1988). All outcrops selected are surrounded on all sides by linear dunes.

Several rock outcroppings, which are used in this study as topographic-obstacles, are identifiable in this sand sea as primarily Tsonab Sandstone Formation but also Sossus Sandstone Formation, (Ward, 1988). The Tsonab Sanstone Formation is a unit of aeolian dune, sand sheet, fluvial, and playa deposits, while the Sossus Sandstone Formation is characterized by aeolian deposits (Ward, 1988). The outcrops range between 4 km to 15 km in length and width (Table 1) and are located within the Namib Sand Sea and are surrounded on all sides by linear dunes.

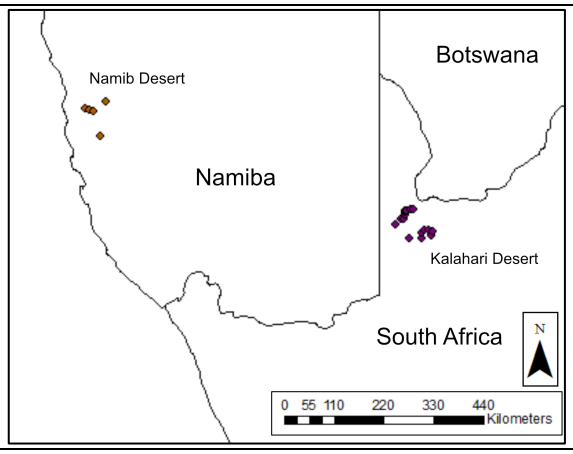

Figure 2a.

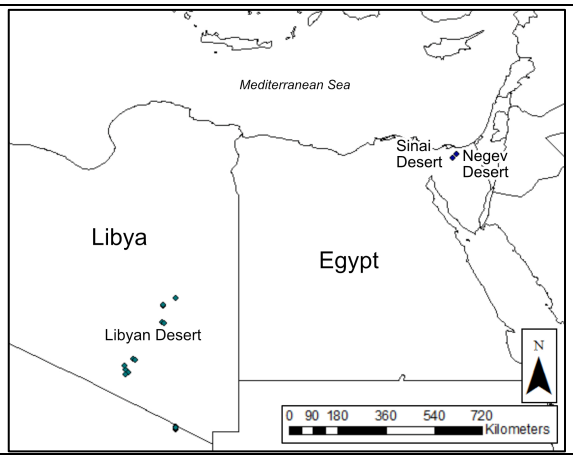

Figure 2b.

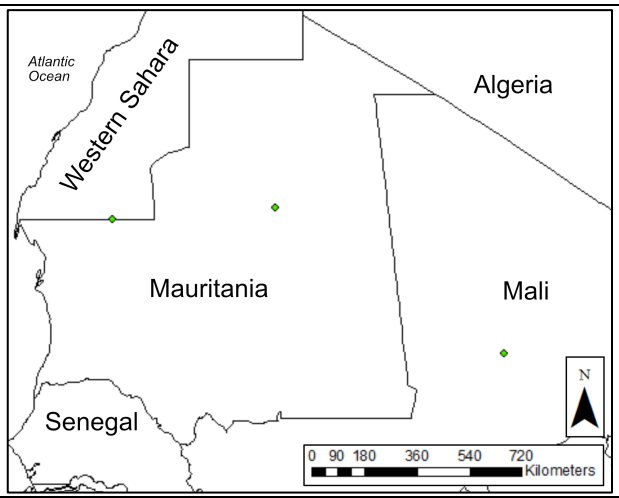

Figure 2c.

Figure 2. Locations of obstacles studied in the Namib and Kalahari (a), Libyan and Sinai (b), and Western Sahara (c) deserts. World country polygon shapefile used is an ESRI provided basemap.

2.2 Kalahari Desert

The Kalahari Desert is a 100-200km wide, semi-arid desert (Figure 2a), spanning parts of South Africa, Botswana, and Namibia (Lancaster, 1988). Linear dunes with a variety of planimetric patterns are oriented northwest to southeast, with some variation, and occupy a majority of the Kalahari Desert (Bullard et al., 1997). The sediment supplying these dunes is thought to originate from the Auob River Valley based on a range of geologic evidence analyzed in Miller (2014), with more southerly paleo-winds likely shaping the present dune field, which is concluded based on a comparison between resultant sand drift direction, which varied greatly by year and location, and modern dune orientations (Bullard et al., 1996). These linear dunes are thought to have formed sometime 32,000 yr B.P., but have since been reactivated at various intervals through time (Lancaster, 1989).

Deflation pans, or small, enclosed basins, spaced at roughly one pan per 20 km occur in the study area and sit below the average interdune elevation. The pans are thought to be ephemeral lakes formed 12 – 20,000 years ago and are characterized today by downwind lunette dunes formed during periods of deflation (Lancaster, 1978; Holmes et al., 2008).

2.3 Libyan Deserts

The Libyan Desert is part of the greater Sahara Desert, and contains a wide range of dune types within the major seas Idhan Murzuq, Ramlat Zaltan, the Great Sand Sea, and the Ramlat Rabyanah which all encompass a range of simple, composite, and

compound dune forms of longitudinal dune type (Lisenbarth, 1991) (Figure 2b). The southern sand seas of the Libyan Desert have not been specifically studied for their age, however, the Sahel, which is found just south of the Libyan sand seas, was constructed between 19 and 15.6 ka with periods of dune reworking more recently (Bristow and Armitage, 2015). Winds are from the north and east (Lisenbarth, 1991). Sediment is fed into the basins within which the Ramlat Rabyanah and the Irq Al Idrisi lie, by alluvial fans from neighboring outcroppings of the African Craton (Charman, 2010; Goudarzi, 1970). Outcrops within the sand seas are likely composed of African Craton material (Goudarzi, 1970).

2.4 Sinai Desert

The Negev and Sinai Deserts contain a 13,000 km2 dune field occupying the northern portion of the Sinai Peninsula in Egypt and Israel (Figure 2b) (Roskin et al., 2011; Tsoar, 1995). Winds for this region blow the strongest in winter from the southwest to northwest directions, with a resultant westerly wind (Roskin et al., 2011). The dunes within this desert range in type, but are dominated by linear dunes (Tsoar, 1983; Rubin et al., 2008) with crestlines oriented east-west for most the northern field, with some northwest to southeast crestlines found in the southwest Sinai Desert, and southwest to northeast trends in the western dune field (Muhs et al., 2013). Most dune formation occurred during the Last Glacial Period with additional aeolian activity occurring during the Pleistocene and Holocene. Sediment supplied to the sand sea is

primarily from the Nile Delta and less substantially from the Wadi El Arish drainage system (Muhs et al., 2013).

Interrupting the flow of dunes is the Gebel Maghara, or Meghara Dome, a carbonate outcropping of Jurassic age (Said and Barakat 1958), which has been chosen as an obstacle for this study. The Meghara Dome is found centrally within the Sinai Desert and has linear dunes found along the north, west, and south sides of the mountain. To the east of the Dome, along east side, are alluvial fans and few to no linear dunes identifiable.

2.5 Western Saharan Desert

The western Sahara Desert comprises a series of northeast to southwest trending linear dune-dominated sand seas including the Azefal, Agneitir, Akchar, and Azaouad that traverse the borders of Mali and Mauritania (Lancaster et al., 2002; Jacobberger, 1989) (Figure 2c). The sand seas across the western Saharan Desert experienced two clear episodes of dune construction during the Late Pleistocene and the later Holocene (Swezey, 2000; Lancaster et al., 2002). Identification of multiple dune trends in the region indicates changes in wind patterns with time (Fryberger, 1980, Lancaster et al., 2002) and present day winds explain the smallest and most recent dune-field patterns (Lancaster et al., 2002).

The Azefal and Akchar sand seas overlie Precambrian basement rock in eastern Mauritania, Miocene-Pliocene rocks near the coast, and the Ageitir sand sea sits on top of the Pleistocene rocks (Lancaster et al., 2002). Based on previously completed

geologic mapping, the obstacles used could be outcroppings of Oujeft Group sandstones, or Atar Cliffs, Nouatil, Teniegouri, and Jbeliat Group sandstones, dolostones, conglomerates, and stromatolitic reefs (Alvaro, 2012; Shields et al., 2007).

3. METHODOLOGY

3.1 Earth analog GIS methods

Five different Earth desert regions were selected based on the presence of both linear, longitudinal dunes and isolated topography that sits within dune field. Within each desert, a minimum of two topographic obstacles were selected. In total, 37 different topographic obstacles were selected (Table 1).

Landsat 8 and SPOT (Satellite Pour I'Observation de la Terre) satellite imagery was used as the base imagery digitize the dunes and topographic obstacles studied on Earth. The imagery used had a spatial resolution between 2.5m to 15m. SPOT provided higher spatial resolution, but had limited coverage and Landsat provided lower resolution, but has worldwide coverage. The imagery used was accessed using the ArcGIS worldwide map.

Advanced Spaceborne Thermal Emission and Reflection Radiometer Digital Elevation Models (ASTER DEMs) were used to examine the topography of the obstacles. ASTER DEMs are a joint Ministry of Economy, Trade, and Industry/ Earth Remote Sensing Data Analysis Center, (METI/ERSDAC) and National Aeronautics and Space Administration/ Land Processes Distributed Archive Center (NASA/ LPDAAC) product composed of 60km by 60km data tiles a standard deviation of vertical error of 12.6 m and a horizontal error between 3 m and 6 m. The DEMs were processed by METI and NASA to remove cloudy pixels and to the remove bad values and outlier values from the DEMs.

For each of the obstacles selected, the crestlines surrounding longitudinal dunes were digitized at least one-half topographic obstacle diameter or more in all directions using GIS software. This was completed using an ArcMap World Imagery basemap of projected in Winkel Tripel. This projection was chosen based on the Tissot indiatrices map projection analysis (Goldberg & Gott III 2007) which preserves shape, orientation, and distance well for the regions in Africa where the dune fields studied are located. The DEMs provided by METI/NASA were in the geoid reference WGS84, and were re-projected into Winkel Tripel. Once these topographic obstacles were selected, obstacle and dune parameters were measured for each topographic obstacle and surrounding dune crestlines. These parameters included obstacle length, width, height, and shadow zone length and dune crest spacing. These parameters are defined in Figure 3a and 3b.

DEMs available for the Earth deserts were used to characterize the three-dimensional morphology of the obstacles. Relief was measured from the interdune height to highest obstacle elevation point and slope was calculated for each DEM grid cell. Slope values were classified with break points at 4, 9, 14, 29, and 75 degrees to normalize the slope maps across all topographic obstacles, and relief was normalized by subtracting the interdune elevation from highest elevation point of an obstacle.

Dune crestlines surrounding each obstacle were subdivided into 50m segments. An azimuthal value for each 50m segment was calculated. The line trend within the 0-180 degree range was recorded. The line data were processed using the ArcMap Near Function (http://help.arcgis.com/EN/ARCGISDESKTOP/10.0/HELP/index.html#//00080000001q

000000) to find the distance from line segment to the nearest topographic-obstacle. These data were subdivided into crestlines found upwind, downwind, and at the corners found between perpendicular and parallel to the resultant wind direction of the obstacles. The corner measurements are denoted as W1, W2, S1, and S2 as shown in Figure 3a and Table 2.

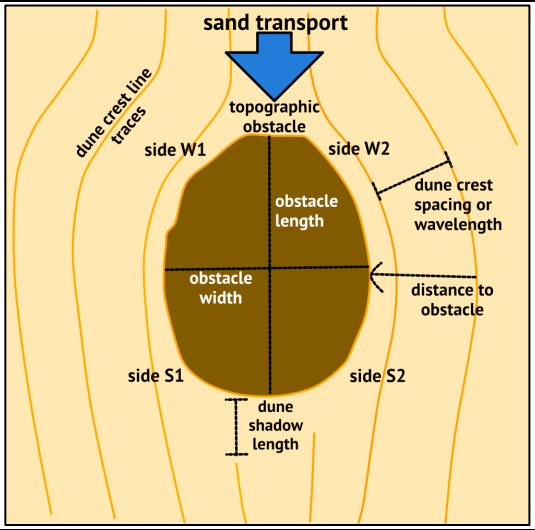

Figure 3a.

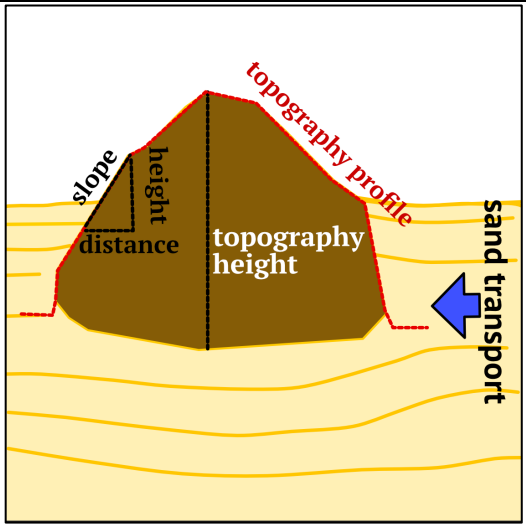

Figure 3b.

Figure 3. Schematic diagram defining how measurements were taken around each topographic-obstacle for this study. Diagram in plan view (a) and profile view (b).

3.2 Wind roses and sand roses

Wind Roses were generated using the NCEP/NCAR Reanalysis Derived data as created by the NOAA (National Oceanic & Atmospheric Administration). The dataset includes the near surface u and v wind vectors, which represent a reanalysis of long-term means for the daily wind measurements for the years 1981 through 2010. These u and v wind vectors represent a Sigma 0.995 level, which is equivalent to an elevation above

the earth's surface that has a 99.5% of surface pressure. As such, this data represents what NOAA refers to as a surface level or roughly 42.2m above the surface (Lileo et al., 2013). The spatial resolution of the data is 2.5 degrees by 2.5 degrees. U and v wind vector values were collected for each topographic-obstacle location. Because of the grid cell size, several obstacles were contained within one cell and, in total, 8 grid cells were analyzed. The u and v data was then used to calculate the resultant wind magnitude and wind direction over the 29-year period (Figure 4a and 4b).

The magnitude and direction values for each location were compiled into rose diagrams using the code created by Daniel Pereira (Copyright © 2015, Daniel Pereira). Because not all winds can mobilize sediment, only wind speeds above the transport threshold value for the smallest reported grain size of each dune field was used. This provides for a wide range of wind data to be analyzed, while recognizing that only a fraction of the winds transport sand. These data were collected from previous field studies at each location. Grain size ranges included 0.1-1 mm for the Libyan Desert (Charman, 2010), 0.18-0.78 mm for the Namib Desert (Lancaster, 1981), 0.21-0.22mm for the Kalahari Desert (Lancaster, 1986), 0.075–1 mm near obstacle M-C (Benito, 1974) and 0.25-0.1mm (Li Sen et al., 1999) in the Western Sahara, and 0.12-0.25 mm in the Sinai and Negev Deserts (Roskin et al., 2014). Using the smallest grain sizes reported for each dune field and the relationship between wind speed, grain size, and threshold of motion established by Bagnold (1942) (Figure 4c), a threshold wind speed was calculated for each of the eight sets. Wind speeds less than the calculated threshold were removed from the wind rose diagrams and the rose diagrams only represent wind

speeds above the fluid threshold. Sediment flux diagrams were generated using the Fryberger and Dean (1979) equation (Figure 4) where a sediment flux was calculated for each 10-degree sector of each rose diagram.

$wind\ magnitude = \sqrt{u^2 + v^2}$ u = x component v = y component	$wind\ direction = arctan\left(\frac{u}{v}\right)$ u = x component v = y component
Figure 4a.	Figure 4b.

$$u^* = A * \sqrt[2]{\frac{\sigma - \rho}{\rho} gd}$$

u* = fluid speed at threshold of motion (m/s)
A = coefficient = 0.1
σ = density of grain = 2.65
ρ = density of fluid (air) = 1.225 kg/m3
g = gravity
d = grain diameter

Figure 4c.

$$q = \frac{V^{*2}\ (V^* - V_t^*) * C''\rho}{g}$$

q =
g = gravity
C'' = empirical constant = 6.7
ρ = density of air = 1.225 kg/m3
V* = shear velocity
Vt* = minimum shear velocity to saltate

Figure 4d.

Figure 4. Equations used for the calculation of wind roses and sand roses. The equation for u* threshold of motion from Bagnold 1942 (a) and the equation for sediment flux modified from Fryberger and Dean 1979.

3.3 Titan GIS methods

Cassini Synthetic Aperture RADAR (SAR) imagery was employed to map dunes and topographic obstacles on Titan. The SAR imagery collected by the Cassini Spacecraft is in the microwave spectrum, with a spatial resolution between 0.35 km and

1.7 km (Elachi, 2004). Although, previous work has derived elevation data using pairs of SAR images with different angles (Callegari et al., 2015), by estimating dune height based on atmosphere thickness (Lorenz et al., 2010), and employing radarclinometry techniques (Neish et al., 2010), no topography data was used in this study of Titan. Only planimetric parameters of the obstacles and dunes were measured and compared to Earth datasets.

Senkyo and Fensal dune fields were chosen based on data availability, data quality, dune crestline visibility, and the presence of isolated topography within the dune field. Criteria for selecting Titan obstacles were identical to those used for Earth. This resulted in a total of 24 obstacles selected for all sand seas on Titan (Table 1). Crestlines were digitized at least one half topographic obstacle diameter or more in all directions away from the obstacle using ArcGIS software. Dune crestlines for each obstacle were subdivided into 400 m segments. 400 m segmentation was selected because of the coarse resolution of the SAR data as compared to the SPOT and Landsat data and because the obstacles on Titan cover eight times the planimetric area as Earth. Thus, the segmentation of crestlines was scaled accordingly. Other manipulations of the line data were done same as with the Earth data described above.

4. RESULTS

4.1 Obstacle morphology: Earth

Obstacles morphologies were classified based on the relief of the obstacle relative to the crest height of the surrounding dunes. Obstacles were identified as positive (Fig. 5a,d) negative (Fig 5b,e) and neutral relief (Fig. 5c,f). Positive topography was defined as at least double the height of surrounding dunes. Neutral topography was defined obstacles with heights approximately the same as the surrounding dunes. Negative topography is lower than the dune height.

In this study, negative obstacles are exclusively associated with deflated playas within the Kalahari. The obstacles range in height between 12 and 50 meters below interdune elevation with an average of 10m below interdune elevation. These obstacles occupy the smallest range of planimetric areas of all obstacle categories studied and range between 0.74 km^2 and 8.83 km^2 (Table 1). Every playa has a rim downwind that rests above interdune elevation at most 30m (Table 1) and extends between 1 and 6.5km along the downwind edge of each playa (Figure 7e). In-board from the rim, the basin is bowl shaped with steepest slopes occurring on the downwind sides at most 7 degrees. Slopes of the rims range between 0 and 35 degrees (Figure 7e, f) and are highest on the downwind side. The obstacle shadow zone of negative obstacles shows an increase in dune spacing along the wind-shielded side of the topography on average 1.67x, and a decrease of 0.93x along the windward side compared to the wavelength of the surrounding field. Negative obstacles have dune occupied obstacle shadow zones.

Within the shadow zone, both lunette dunes and linear dunes form directly adjacent to the wind-shielded side of the obstacle in most instances (Figure 8a, b). The increased dune crest wavelength found immediately behind the obstacle transitions back to a wavelength that matches the surrounding dune field within 8 km from the edge of the obstacle, but frequently less. Unlike other obstacles, the shadow zone does not sit below the interdune elevation, but rather is at the interdune elevation (Figure 5d).

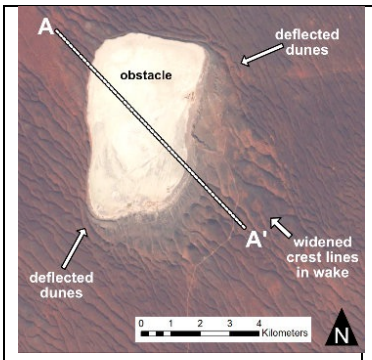

Figure 5a.

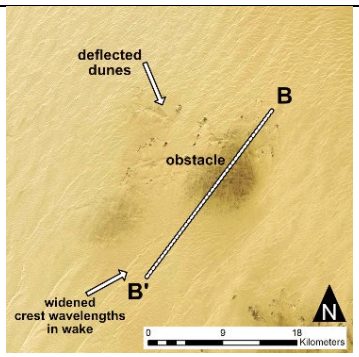

Figure 5b.

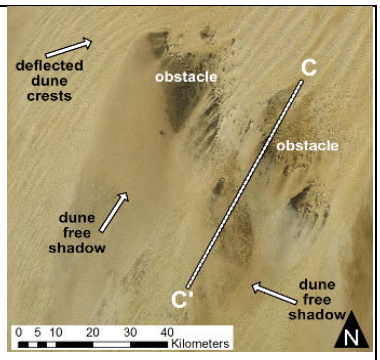

Figure 5c.

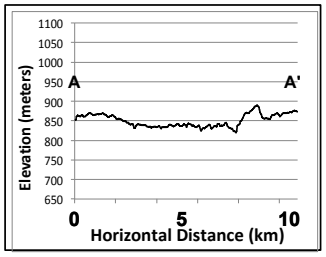

Figure 5d.

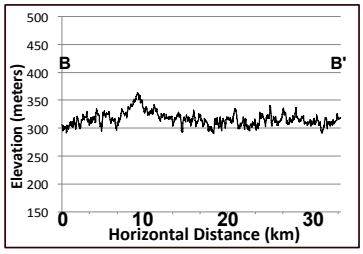

Figure 5e.

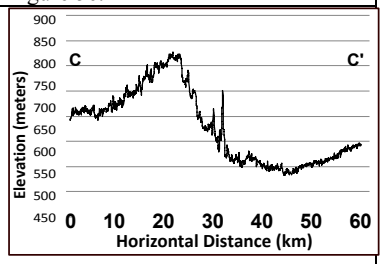

Figure 5f.

Figure 5. 15m resolution Landsat satellite image of a negative relief obstacle in Kalahari (a), a neutral relief Libyan obstacle (b), and a positive relief Libyan obstacle (c) with elevation profiles for the negative (d), neutral (e), and positive (f) relief obstacles displayed directly below them.

Figure 6a.

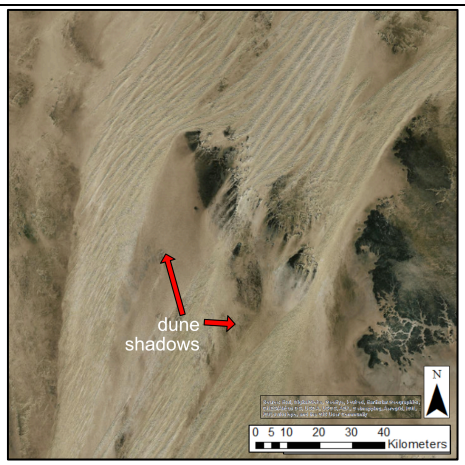

Figure 6b.

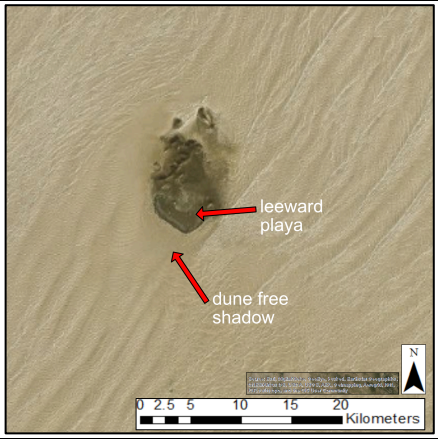

Figure 6c.

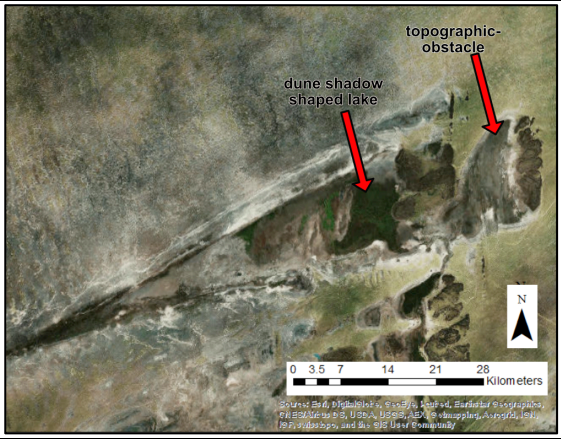

Figure 6d.

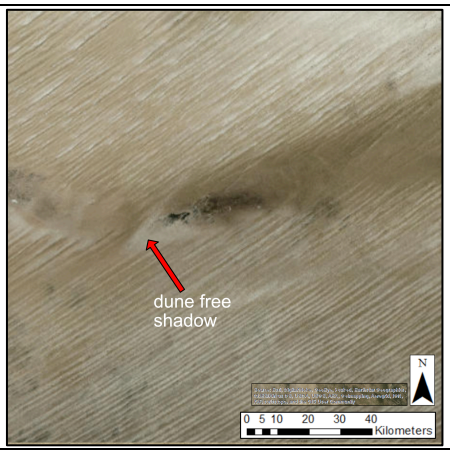

Figure 6e.

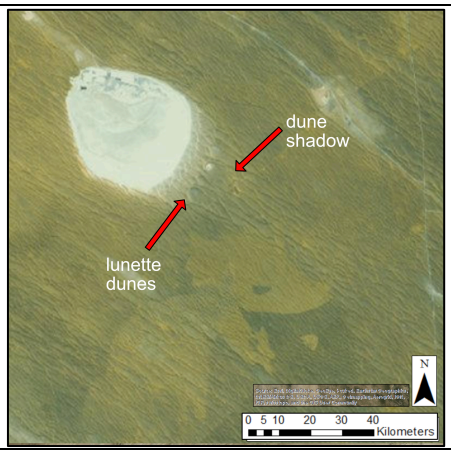

Figure 6f.

Figure 6. 15m resolution Landsat satellite image of a positive relief, Namib obstacle (a), positive relief Libya obstacles (b,c), a dune-shadow shaped lake found in a depression along the wind-shielded side of an obstacle in Mali near Timbuktu (d), and neutral relief, Kalahari obstacles (e,f).

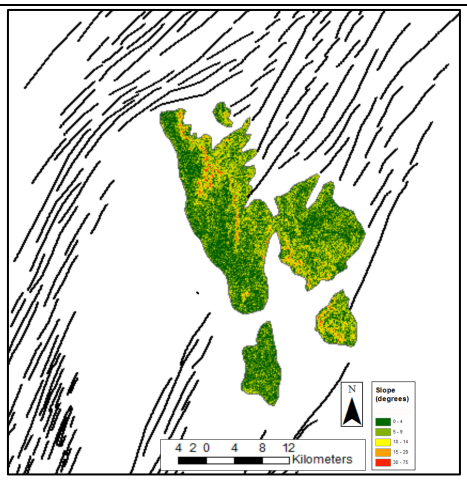

Figure 7a.

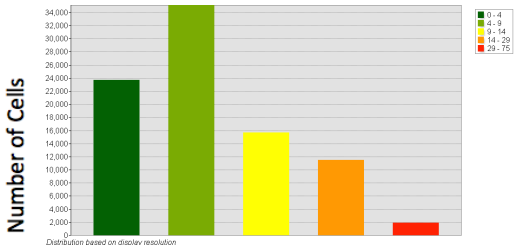

Figure 7b.

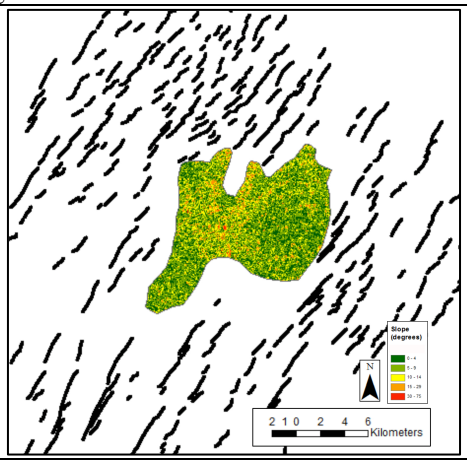

Figure 7c.

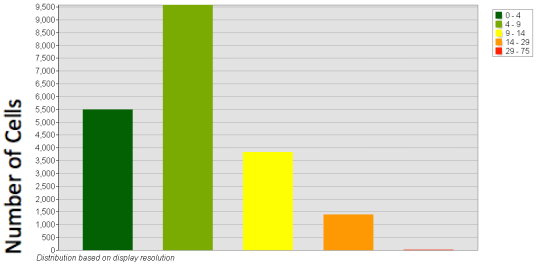

Figure 7d.

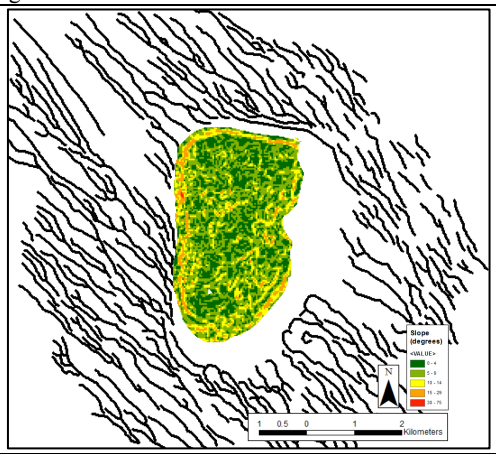

Figure 7e.

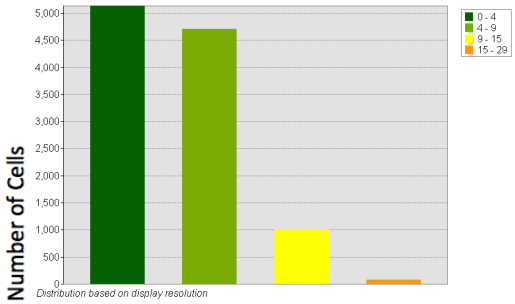

Figure 7f.

Figure 7. Slope parameter maps with associated slope values of a neutral relief obstacle in Libya (a, b), positive relief obstacle in Libya (c,d), and a negative relief obstacle in Kalahari (e,f).

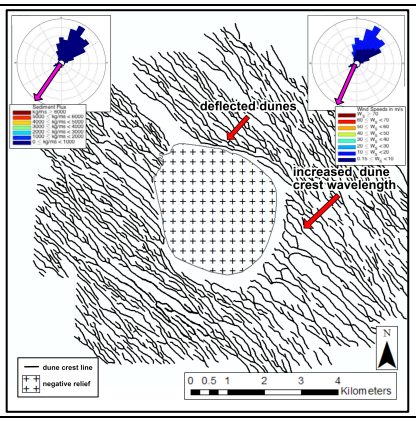

Figure 8a.

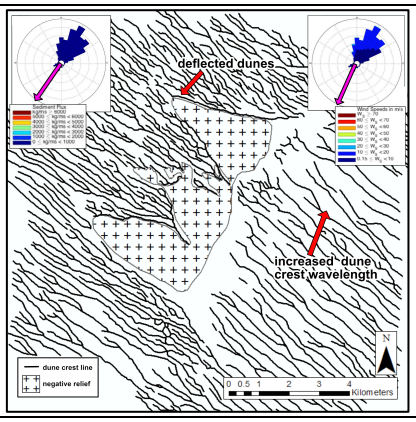

Figure 8b.

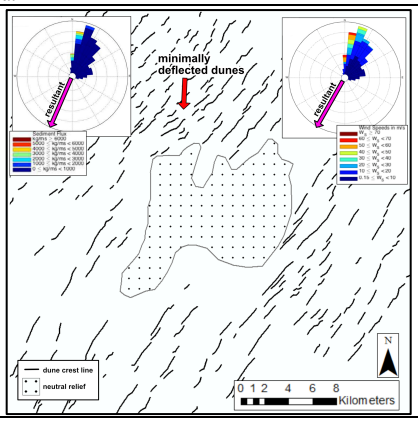

Figure 8c.

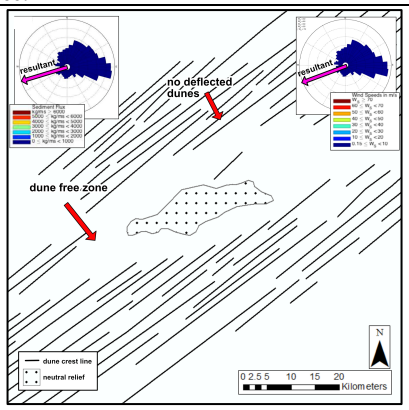

Figure 8d.

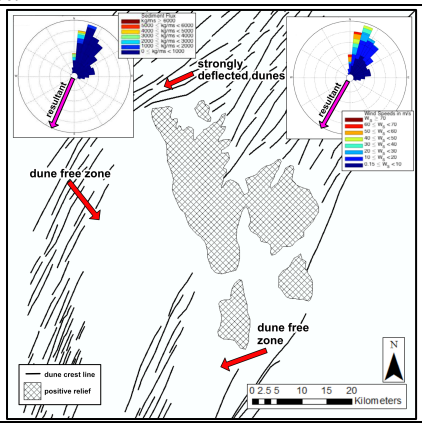

Figure 8e.

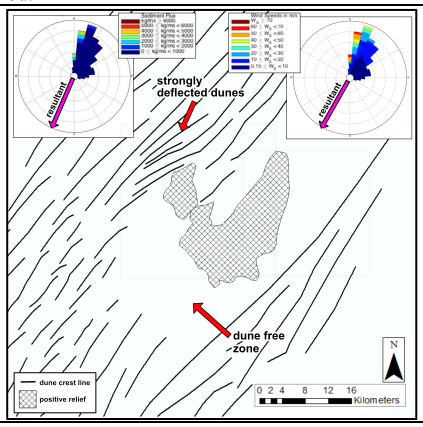

Figure 8f.

Figure 8. Digitally polygoned negative relief obstacle in Kalahari (a,b), neutrl relief obstacles from Libya (c) and Mauritania (d), positive relief obstacles in Libya (e,f). Top right inset is a wind rose. Top left inset is a sand flux diagram. Resultant sand rose and sand flux vectors are plotted on top of the roses respectively.

Neutral obstacles represent outcroppings in our study. These obstacles fall between 51 and 164m above interdune elevation, with an average height of 39m, and dip below interdune elevation at most 81m (Table 1). Neutral obstacles represent a narrower range of planimetric areas between 20.9 km^2 and 175.0 km^2 when compared to positive obstacles, but occupy greater areas than negative obstacles. These obstacles range in slope between 0 and 46 degrees but are dominated by slopes in the 4-9 degree range, and a few slopes in the 29-75 degree range (Figure 7c, d). Obstacles categorized as neutral are associated with an obstacle shadow zone along the wind-shielded face (Figure 6e). For neutral obstacles, the obstacle shadow zone typically does not have dunes immediately behind the wind-shielded obstacle face, but develops dunes one dune crest wavelength or two at most behind the obstacle, and returns to dune field mean within 22 km. Dune crest wavelength is an average 1.47x the surrounding dune field mean along the wind-shielded side, and 0.79x along the windward side. Furthermore, there is no depression found on the wind-shielded side (Figure 5e).

Positive obstacles chosen for the study represent outcroppings through mountains. These topographic features range in height between 121m above interdune elevation and 729 m, with an average height of 294 m (Table 1). Positive obstacles represent the widest range in planimetric area of all obstacles studied, from 2.7 km^2 to 437.4 km^2. The topography occasionally dips below interdune elevation by at most 44m, with slopes ranging between 0 and 59 degrees. Slope values are dominated by values in the 4-9 degree range, but positive obstacles have a higher percentage of slopes within the 29-75 degree range than neutral or negative obstacles, with a concentration of high

slopes along the windward side (Figure 7a,b). Along the windward side dune wavelength is .62x to 1.03x dune field mean, while the wind-shielded side wavelength is 1.05 – 1.28x field mean. For the positive obstacles associated with an obstacle shadow zone that is completely void of dunes, the obstacle shadow zone is widest on the wind-shielded side of the obstacle, and narrows to a point downwind of the obstacle. The length of the shadow zones varies greatly from obstacle to obstacle across all the study areas, between 1.3 km and 58.5 km (Table 1). Shadows that are void of dunes altogether, such as in Libya (Figure 8e) or Western Sahara (Figure 8d), are also associated with a depression on the wind-shielded side of the obstacle that varies in depth from obstacle to obstacle between 20 and 44m below interdune elevation.

In addition to variation in the obstacle relief, the geomorphology associated with the different obstacles is highly varied. All obstacles within the Namib were flanked on all sides by large alluvial fans before giving way downslope to the dune field (Figure 6a), while Libyan obstacles had a few, isolated alluvial fans. Obstacles within the Kalahari and the Western Sahara had no alluvial fans. Furthermore is the inferred amount of material piling found along the windward side versus the wind-shielded side for various obstacles. For all positive obstacles and some neutral obstacles studied in Libya, West Sahara, and Namib there is a gradual increase in landscape elevation on the windward side, which drops directly behind the obstacle's highest slopes or sharpest peaks into a depression (Figure 5c, 5f). Additionally, there is sand found to occupy the region right up to or against the high slopes windward, which are not present along the

wind-shielded side. This relationship in slope trends is not true for the Kalahari, negative obstacles.

The geomorphology of dune-free shadow zones of the obstacles also varied greatly. All obstacles within the Namib had dune-free shadow zones (Figure 6b). Although the dune-free shadow zones in the Namib are covered by sandsheets, obstacle shadow zones in Libya are characterized by evaporite playas (Figure 6c) and alternatively sand sheets. In yet another example, standing water existed within the dune-free shadow zone (Figure 6d) in the Western Sahara. In other Western Sahara studied examples, obstacle shadow zones were defined by playas or sand sheets with isolated patches of vegetation. Overall the range of geomorphic environments recognized within the dune-free shadow zones studied included sandsheets, standing water, playas, vegetation, or some combination among those geomorphologies.

4.2 Obstacle morphology: Titan

Target obstacles on Titan for this study exhibit a broad range of planimetric morphologies and have been interpreted as topographic obstacles based on the radar bright, or rough, appearance of these features in SAR imagery (Elachi et al., 2006; Radebaugh et al., 2007) (Figure 9). These obstacles range in size between 1 to 33 km in width and 3 to 130 km length with a range in planimetric area between 21.4 and 3149.8 km^2 (Table 1).

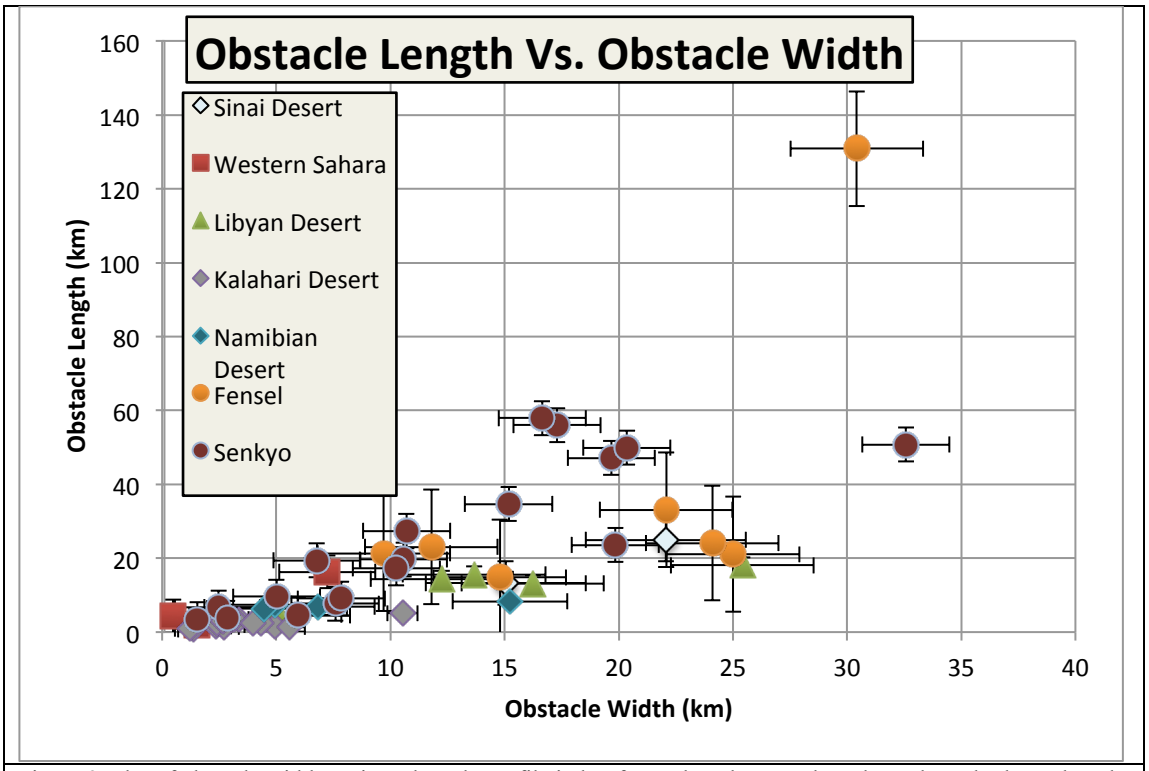

Figure 9. Plot of obstacle width against obstacle profile in km for each and every obstacle study on both Earth and Titan. Not the Titan obstacles occupy more of the larger width to profile sizes than the Earth obstacle analogs.

On Titan no wind data is available and the obstacle shadow zones are inferred to be radar bright zones within which no dune-shaped radar dark surfaces are visible and

which extend in the direction of the linear dune crestline orientation. These radar bright areas vary in brightness giving a mottled appearance, which results from a combination of the incidence angle of the SAR microwave signal and the backscatter efficiency of the imaged material (Elachi, 2004). As such, previous studies have interpreted the RADAR bright areas to be rough, rocky terrain while the dark absorbing areas are interpreted to be smooth absorbing features such as dunes (Lorenz et al., 2006; Radebaugh et al., 2008; Elachi et al.,2006., 2010; Mastrogiuseppe et al., 2014). Based on the criteria of dune free regions, a shadow zone occurs on the east side in 8% of studied obstacles. However, defining the shadow zone to be a region where an increase in dune wavelength and a greater exposure of the radar bright, interdune material exists, 92% of the obstacles measured in Fensal and Senkyo dune fields having dune occupied obstacle shadow zones on the east side.

4.3 Crestline modification around negative obstacle relief

The range of crestline deflection around negative relief obstacles varies between 0 and 70 degrees. 82% of the deflected dunes occur within 3 km of the pan (Figure 10), which is 18 dune wavelengths from the pan. However, for the windward side dune orientation returns to dune field mean between 1 – 4 wavelengths. Beyond 3 km from the obstacle sides, dune orientation begins to recover to the mean dune field orientation of 127 degrees. This contrasts with positive and neutral obstacle types where reorientation ranged up to 70 degrees (Figure 8).

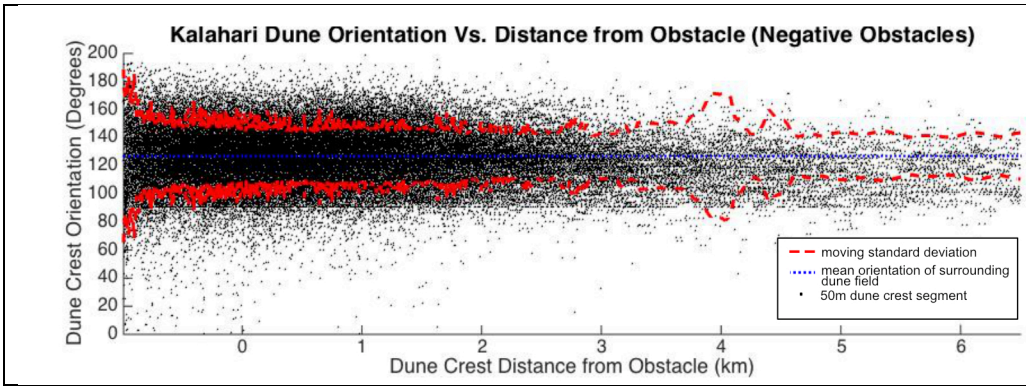

Figure 10. Plot of dune crests azimuthal orientation values subdivided into 50m segments against the how far the dune crest is away from the obstacle. This plot depicts dunes around negative relief obstacles in the Kalahari Desert only.

Crest wavelength varies by position around the obstacle. Dunes adjacent to the windward side of the obstacle have an average wavelength of 158.5m, which is 93% of the mean wavelength of the surrounding longitudinal dune field at 170m. Within 1 km of the obstacles windward edges, wavelength decreases to an average of 81% and 64% wavelengths respectively (Table 2a) with a coincident high-degree of reorientation (Figure 10). Dune wavelength increases along the southeast and south edges, as well as immediately downwind of the obstacle to between 1.1x and 1.7x field-mean wavelength (Table 2a). The distance between the downwind edge of the obstacle and a return to field-mean dune spacing and orientation varies by locality between 0.7 and 8.3 km (Table 1). Dune crestlines returned to the field-mean wavelength at 2.0-2.5 km for the windward side recognized by the narrowing of the distribution of wavelengths at 2.5 km from the obstacle(Figure 10). Dunes on the wind-shielded side gradually return to field-mean orientation at around 5.5 km.

4.4 Crestline modification around neutral obstacle relief

Crestlines adjacent to neutral relief obstacles typically recover to the field mean orientation at a shorter distance, measured in dune wavelengths, from the obstacle than all positive and most negative obstacles. Dune crestline reorientation occurs up to 5 km or 3 field-mean wavelengths from the windward obstacle edge (Figure 8c), but most are modified within 3 dune wavelengths and, more typically, not modified at all (Figure 8d). A comparison between crestline orientation and distance from obstacle demonstrates crestline reorientation ranges from 10 degrees (e.g., Western Sahara, Figure 11b) to 45 degrees (e.g., Libya, Figure 11a) from the field mean and within our estimated error range of crestline orientation mapping.

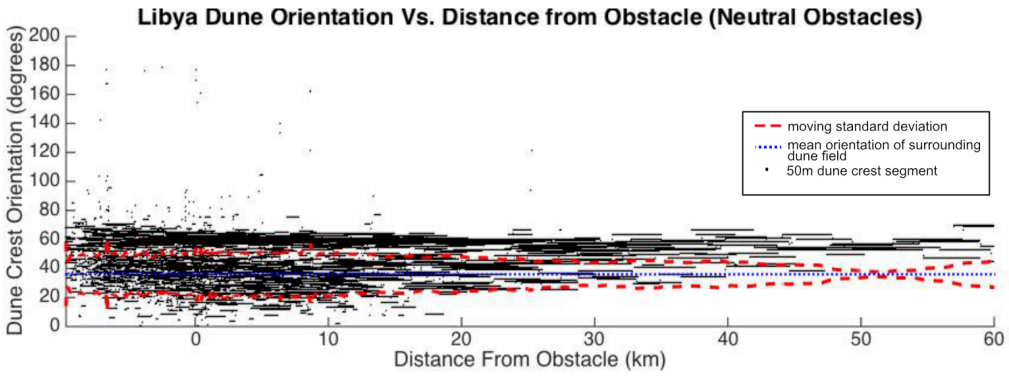

Figure 11a.

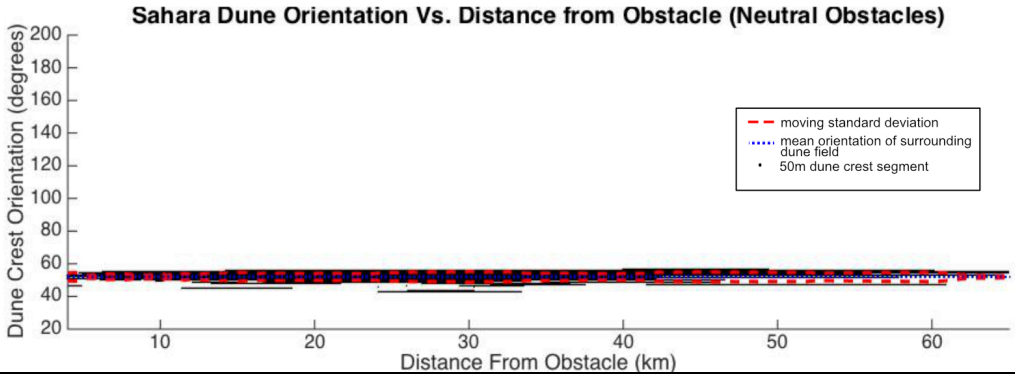

Figure 11b.

Figure 11. Plots of dune crests azimuthal orientation values divided into 50m segments against how far the dune crest is away from the obstacle. Plots depict neutral relief obstacles only for Libya (a) and Sahara (b).

As with negative relief dune-obstacle interactions, the dune crest wavelengths vary depending on proximity and location relative to the obstacle. The crestline wavelength along the windward face of the Sahara study areas shows a slight increase in wavelength at 103% of the field mean, whereas the Libya desert study area shows a decrease in wavelength at 93% of the field mean (Table 2a). Neutral relief obstacles are associated with an increase in crest wavelength on the wind-protected side of the obstacles, however there is a region 1 – 3 wavelengths in length where no dunes are present behind the obstacles (Figure 7b). For neutral relief obstacles, the obstacle shadow zone also varies widely from obstacle to obstacle, between 3.0 and 39.0 km (Table 1).

4.5 Crestline modification around positive relief obstacle

Positive relief obstacles can be found in the Libyan Desert, Sinai Desert, Western Sahara Desert, and Namib Desert. The relationships and interactions between the surrounding dune field and positive relief obstacles are not unlike those found for negative and neutral relief obstacles, but can still be characterized independently.

Among the negative, neutral, and positive relief obstacles, positive relief obstacles are associated with the greatest amount of dune crest deflection between 4 and 7 crest wavelengths out from the topographic-obstacle (Figure 8e and 8f) or at most 15 km on the windward side. Yet, crestlines do not reorient the dunes away from the surrounding dune field orientation more than 60 degrees for most study areas plotted (Figure 12a, b, c, d). Furthermore, the change in dunes from reoriented away from the field mean to matching dune field mean occurs along the windward side at roughly 20 km, but this transition occurs nearer 30 km away along wind-shielded side in the Sahara (Figure 15d), with a similar but less marked trend observable for the Sinai obstacles of 11km and 13 km respectively (Figure 15b).

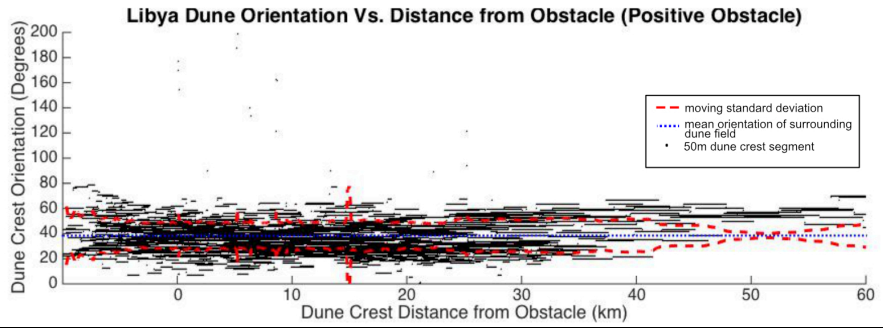

Figure 12a.

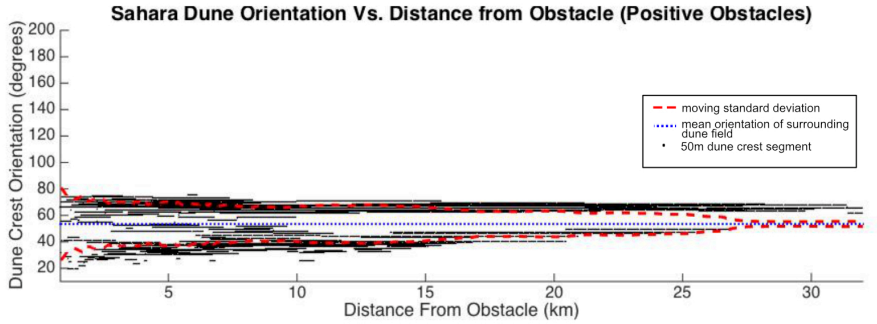

Figure 12b.

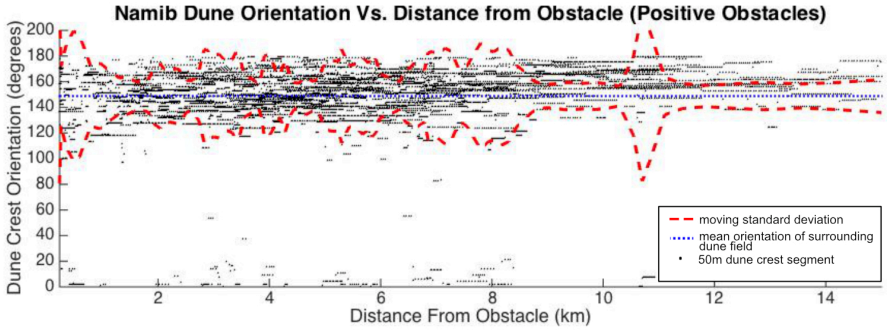

Figure 12c.

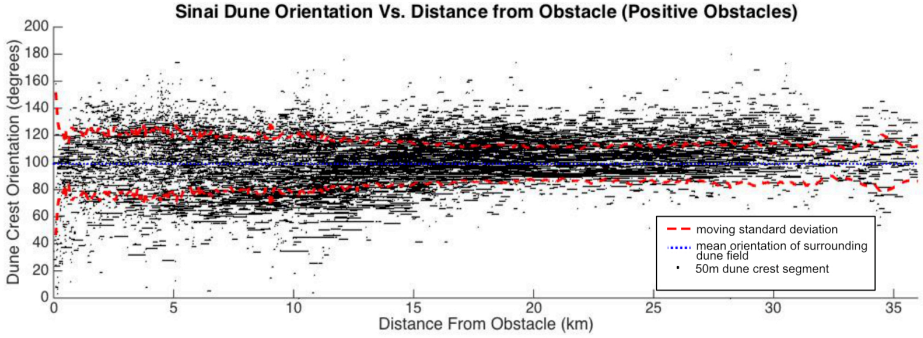

Figure 12d.

Figure 12. Plots of dune crests azimuthal orientation values divided into 50m segments against how far the dune crest is away from the obstacle. Plots depict dunes around positive obstacles in Libya (a), West Sahara (b), Namib (c), and Sinai (d).

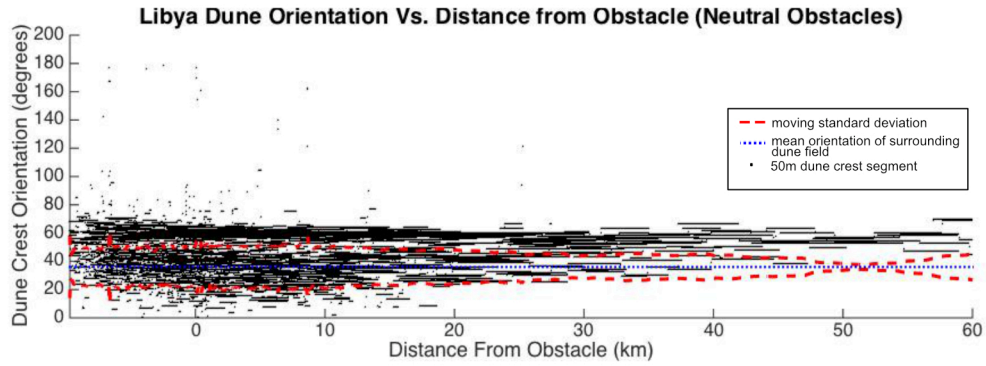

Figure 13. Plot of dune crests azimuthal orientation values subdivided into 50m segments against the how far the dune crest is asway from the obstacle. This plot depicts dunes around neutral relief obstacles in the Libyan Desert only.

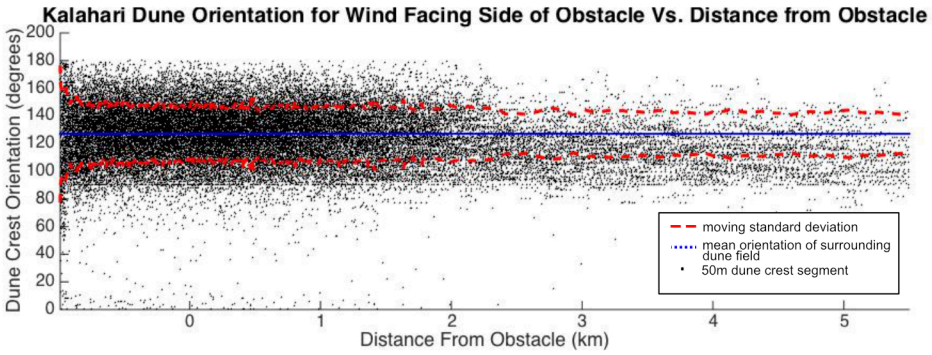

Figure 14a.

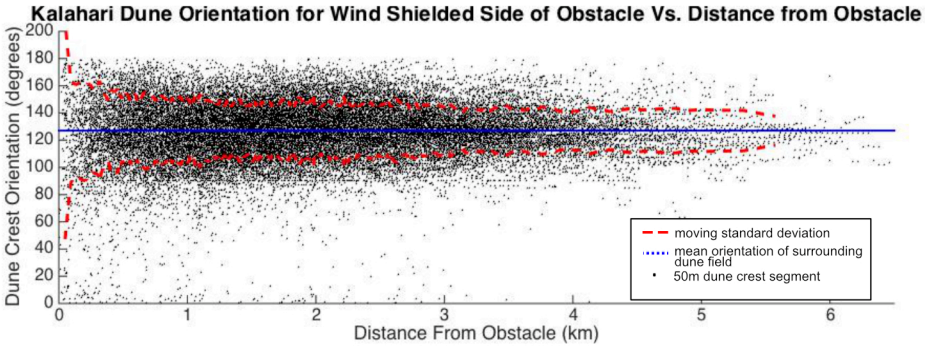

Figure 14b.

Figure 14. Plots of dune crests azimuthal orientation values divided into 50m segments against how far the dune crest is away from the obstacle. . Plot depicts dunes around neutral obstacles in Libya.

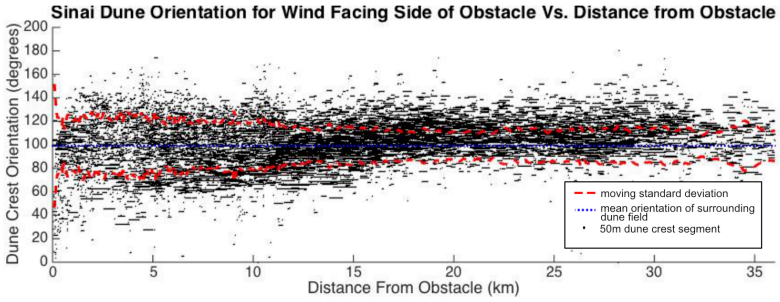

Figure 15a.

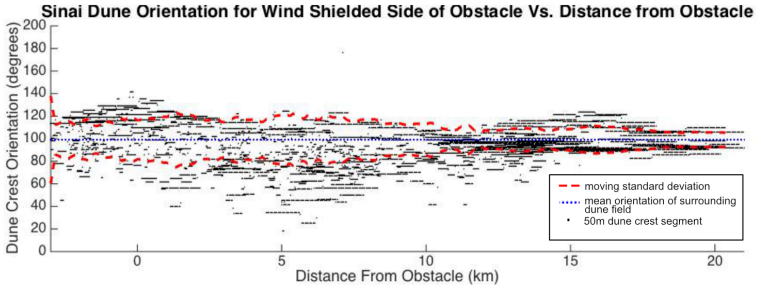

Figure 15b.

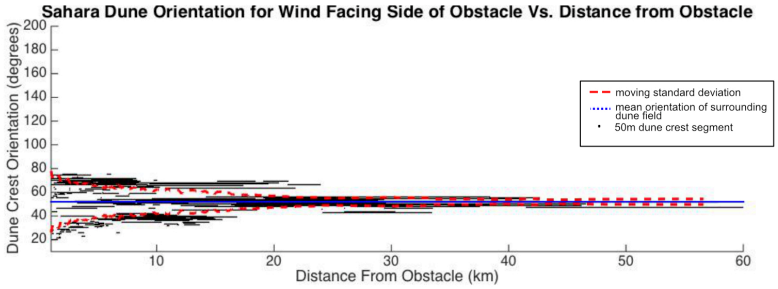

Figure 15c.

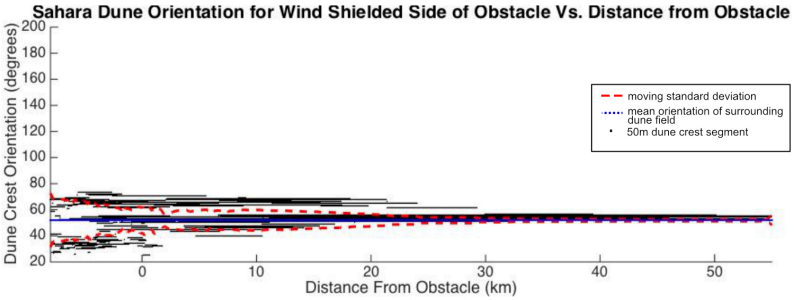

Figure 15d.

Figure 15. Plot of dune crests azimuthal orientation values subdivided into 50m segments against the how far the dune crest is away from the obstacle. This plot depicts dunes around the wind facing side of the obstacle (a,c) and the wind shielded side of the obstacle (b,d) for the Sinai and West Sahara obstacles respectively.

Similarly to the negative and neutral relief dune-obstacle interactions, there are different wavelength changes dependent on dune crest location relative to the obstacle. Crestlines near the windward face are on average between 62% and 103% of dune field mean, while the wind-shielded dunes between 105% and 128% field mean dependent on desert area. As such, positive obstacles have more closely spaced dunes along the windward face and larger wavelengths along the wind-shielded face coincide with the faces of the obstacles that experience the highest wind exposure are associated (Figure 12 a, b, c, d). Like other obstacle relief types, the further away from the obstacle, the more dune crestlines match the orientation and wavelength of the unmodified dune field. Furthermore, all positive relief obstacles are associated with either a dune free, obstacle shadow zone and coincident landscape depression on the wind-shielded side of the topography (Figure 8e, f) or alternatively greater wavelength dune crests.

4.6 Crestline modification in Fensal and Senkyo dune fields

Many of the same observations can be made for the Titan dune fields of Fensal and Senkyo as can be made for their Earth counterparts. However, without elevation data, Titan's dune-topography interactions do not have the context of obstacle morphology (that is positive, negative, or neutral relief). Nonetheless, there exist comparable relationships to the dune-topography interactions on Earth.

First, dunes are reoriented more proximally to an obstacle than are distally, as can be seen by graphing the dune crestline orientation against distance the dune is from the obstacle (Figure 16). Second, the west side of the obstacles the dune reorientation

returns to field-mean by 50-60 km out in the Senkyo field (Figure 16a), yet to the east side the dune crests do not match the surrounding dune field orientation until 90 – 100km away from the east edge (Figure 16b), with a similar trend seen in the Fensal plots (Figure 16c and 16d).

Second, most dune-topography interactions show an increase in wavelength of crest lines along the eastward side of the obstacles (Table 2b). The east side shows a dune wavelength change between 104% and 106% when compared to the field mean wavelength. However, along the west side of the obstacles dune wavelength decreases between 98% and 83% of dune field mean. Along the northeast, northwest, southeast, and southwest edges of obstacles, a decrease in crest wavelength is observable, between 75% and 98% of the surrounding average dune field wavelength. As with the Earth analog obstacles, the obstacle shadow zone length varies widely from obstacle to obstacle between 3.2 and 42.3 km in Fensal and 3.7 to 47.4 km in Senkyo (Table1).

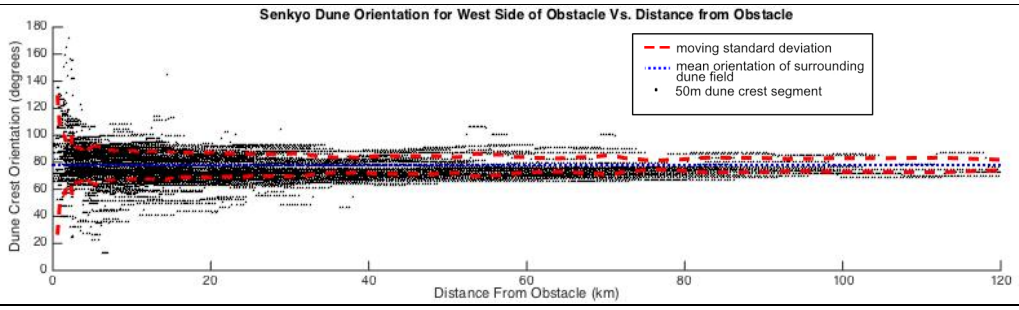

Figure 16a.

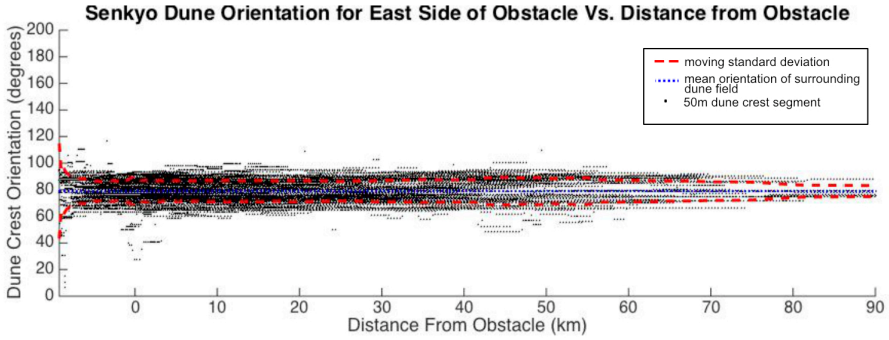

Figure 16b.

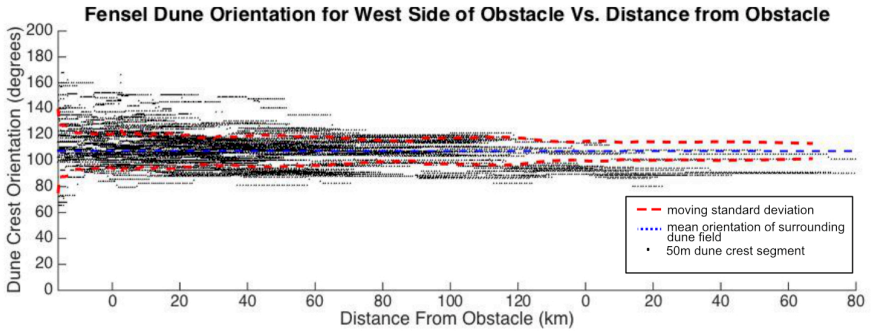

Figure 16c.

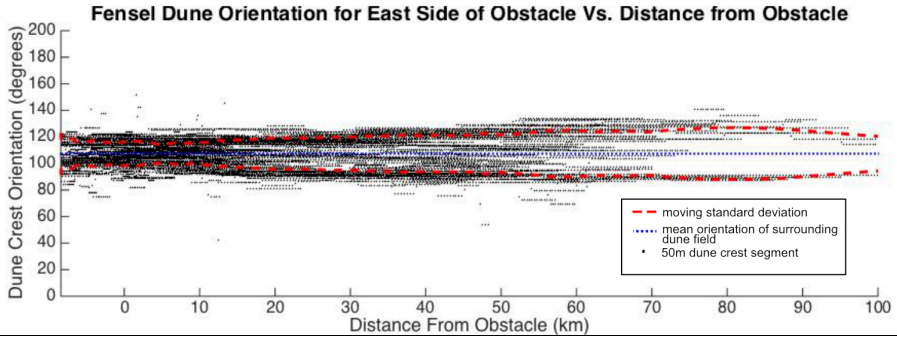

Figure 16d.

Figure 16. Plot of dune crests azimuthal orientation values subdivided into 400m segments against the how far the dune crest is away from the obstacle. This plot depicts dunes around the west side of the obstacle (a,c) and the east side of the obstacle (b,d) for the Senkyo and Fensal obstacles respectively.

5. DISCUSSION

Do dune-obstacle interactions show a signature of wind speed and wind and sand transport direction? Researchers have compared the appearance of Titan's linear dune-obstacle interactions to similar features on Earth (Radebaugh 2013, 2010; Lorenz et al., 2006; Neish et al., 2010), but have not examined the variability among the dune-obstacle interactions, the formative processes, or the reliability of morphology to interpret winds or sand transport direction. This study examines a range of topographic obstacle morphologies and the resulting dune-patterns around obstacles in order to develop hypotheses about the formative mechanisms and application to interpreting Titan's aeolian equatorial landscape.

5.1 A review of obstacle-influenced dune types

A wide range of obstacle-modified dunes occur on Earth as a consequence of the interaction between winds and topographic obstacles. Recognizing these dune types and the formative mechanisms of these dune types provides a basis to evaluate the type of dune-obstacle interactions on Titan. Obstacle-modified dunes include echo dunes, sand drifts, lee dunes or sand shadows, climbing dunes, falling dunes, and sand ramps (Lancaster and Tchakerian, 1996; Xiao et al., 2015; Xianwan et al., 1999; Tsoar, 1983). Echo dunes form upwind of obstacles via a reverse-flow eddy resulting from the interaction of the wind and the obstacle (Tsoar, 1983). Sand drifts form in the lee of two adjacent obstacles as a result of the deceleration of flow downwind of the gap between

two obstacles (Luo et al., 2014; Bagnold, 1942). Lee dunes or sand shadows form in the wind-sheltered lee of an obstacle and can extend parallel to the wind into a linear dune ridgeline (Figure 17a). (Xiao et al., 2015; Bagnold, 1942). Climbing and falling dunes, also called mountain dunes, migrate up and down a gently sloped terrain (Xianwan et al., 1999) (Figure 17c and d). Sand ramps are the buildup of sediment up against the windward side of an obstacle primarily by aeolian but additionally by deposition of fluvial and talus processes (Lancaster & Tchakerian, 1996) (Figure 17b). Although this suite of obstacle-modified dunes may exist on Titan, the scale of these dune types on Earth, with the exception of lee dunes, is below the spatial resolution of Titan SAR data. Lee dunes, which form at a scale detectable by the Titan SAR data typically develop as a singular, elongate dune in the lee of an obstacle. The linear dunes observed on Titan are found to populate all sides of obstacles, thus lee dune formation alone cannot explain the range of observed morphologies on Titan. At the dune-field scale, Titan's dunes appear to reflect regional sediment supply, sediment availability and wind conditions rather than localized conditions created by obstacles as with other obstacle modified dunes. Similar to obstacle-modified dunes, however, dune-field patterns adjacent to the obstacle appear to be modified by the size, shape and slope of the obstacle, which in turn, modify wind flow and sediment availability.

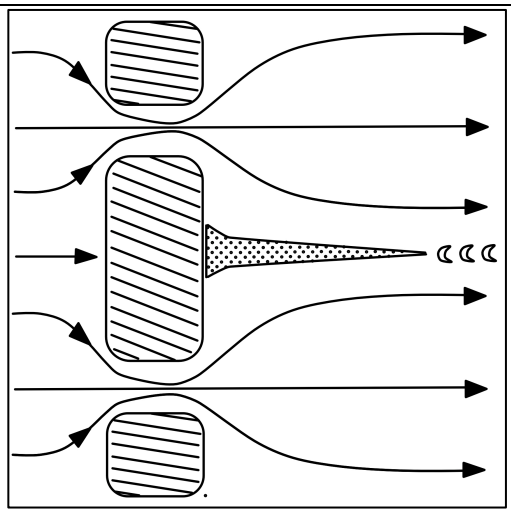

Figure 17a.

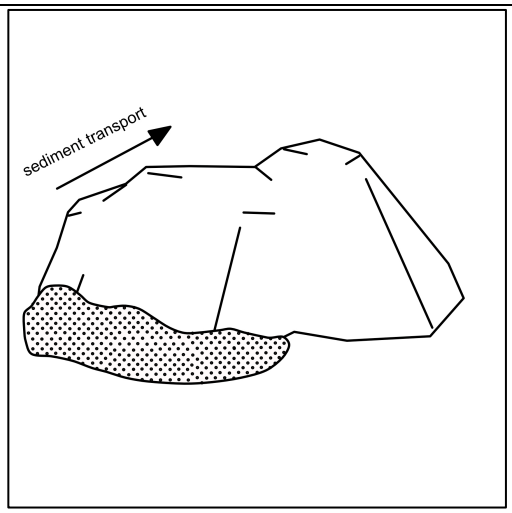

Figure 17b.

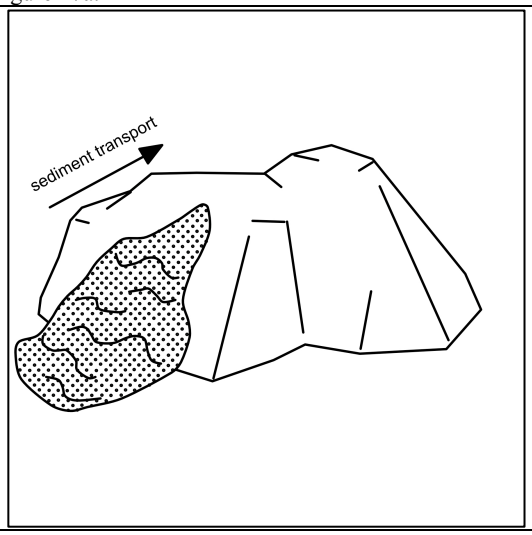

Figure 17c.

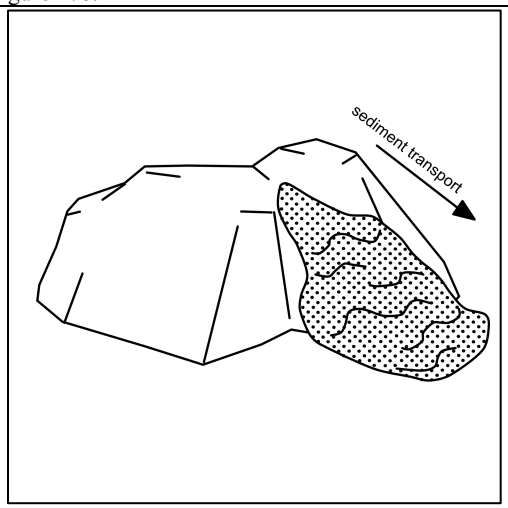

Figure 17d.

Figure 17. Schematic diagrams depicting obstacle-influenced dunes, including sand drifts modified from Luo et al., 2014 (a), sand ramps based on the descriptions of and figures in Lancaster & Tchakerian 1996 (b), and mountains dunes, that is climbing (c) and falling (d), modified from Xianwan et al. 1999.

5.2 Formative mechanisms obstacle morphology and dune patterns

The topographic characteristics that appear to most strongly influence the dune patterns adjacent to an obstacle are the magnitude of the relief of an obstacle and the windward slope of an obstacle. Why does windward slope modify dune orientation? As

with echo dunes, reverse and deflected wind flow is expected at the windward side of an obstacle. The modification of wind conditions could in turn locally affect dune orientation, however, detailed observations of dune-modification around obstacles reveals that dunes, which are clearly impacted by flow modification, only occur within a 500 m of the obstacle (Cisneros, 2014) for a 2 km by 4 km obstacle. This suggests that wind modification by the obstacle alone effect cannot account for crestline deflection several kilometers away from the obstacle as we have observed.

Upwind reverse wind flow would also promote sand deposition upwind of the obstacle. The magnitude of the flow reversal depends on the windward facing slope and wind strike angle such that higher slopes promote more sand deposition (Qian et al., 2011, Tsoar, 1983). In turn, more sand deposition upwind of the obstacle changes sediment availability and forces the pattern modification away from the obstacle. In contrast, obstacles with a more gently sloped windward slopes would promote the bypassing of sediment around the obstacle and result in less pattern modification.

The relationships between obstacle windward slope, wind strike angle, and wind velocity have been determined both mathematically and experimentally to play a role in how material interacts with an obstacle. These parameters in conjunction determine whether sediment is exclusively deposited along the windward slopes of an obstacle, both deposited and carried up the windward face, or solely transported up the windward face in the form of climbing dunes. Tsoar (1983) experimentally and mathematically determined that a stagnation point occurs along windward slopes of 38 degrees or greater. Below the stagnation point a reverse eddy forms depositing material on the

windward face and above which flow passes over the obstacle. Furthermore, these experiments demonstrated that the higher the windward slope, the greater the amount of material was deposited windward at a constant wind speed. Thus, when considering windward slope and a constant flow speed alone, obstacles with slopes 38 degrees or greater will accumulate material along the windward face. Xianwan (1999) considered changes in flow speed and strike angle of the wind. The study's experimental approach demonstrated that greater wind strike angle, greater windward slopes, and lower wind speeds result in more windward deposition. Notably, material can accumulate along the windward slopes of an obstacle with slopes lower than 38 degrees given a high enough wind strike angle. Xianwan (1999) experimentally found windward deposition can occur at slopes as low as 30 degrees but higher than 15 degrees if the wind strike angle is sufficiently high or wind speed sufficiently low.

These previous studies provide some possible context to what is observed in the studied obstacle dune interactions, where greater windward slope angles resulted in greater reorientation of dunes laterally. This could offer an explanation as to why the positive obstacles, with up to 59 degree windward slopes saw the greatest reorientation of dunes at 4 – 7 crest wavelengths, where the higher slopes promoted a greater amount of material deposited windward, resulting in more material forced laterally to reorient dunes further out. By extension, the neutral obstacles, which have low windward slopes, most in the 4 – 9 degree range (Figure 7d), show minimal to no deflection of dune crests.

The negative obstacles, despite the proximally reoriented dunes, do not have slopes sufficiently high enough along the windward edges to result in the deposition of

material and by extension the lateral reorientation of dune crestlines. As such, the model we propose for neutral and positive obstacles does not work for our negative relief obstacles. Yet, previous studied have established that negative relief landforms within the Kalahari, specifically dried river valleys, are associated with the deflection of dune crests (Bullard et al., 1995). Previous work suggests that the modification of wind flow as well as sediment supply that results from the river valleys presence could explain the modification of dune field patterns (Bullard et al., 1998). While the modification of wind flow does not work at the larger scales associated with the neutral and positive obstacles, the negative obstacles are small enough to work with more current obstacle modified flow studies (Cisneros et al., 2014).

5.3 Variations in the shadow zone behind obstacles

Although dune deflection around an obstacle is a defining characteristic of the dune-obstacle interactions, the dune-free shadow zones that form on one side of an obstacle are widely used to infer wind and transport direction. Are dune-free shadow zones typical of the leeward side of obstacles? The results show that dune-free zones correlate strongly with positive relief obstacles and form downwind of an obstacle in the resultant wind and sand transport directions (Figure 8e,f). The heights and slopes of the obstacles imply the shadow zones form from a sediment shielding mechanism whereby sediment is simply blocked from deposition behind the obstacle, rather than removal of sediment through wind modification by the obstacle. Interestingly, in an obtuse bimodal wind, sand deposition behind the obstacle would be expected as sediment is moved into the

shadow zone from the sides (Cisneros et al., 2014) for a 2 km by 4 km obstacle. However, the size and shape of the shadow zone does not appear to vary with wind regime alone, which suggests other boundary conditions such as sediment supply, sediment availability, the presence of a near surface water table, and vegetation, may control the size and shape of the shadow zone.

In many instances a depression occurred within the dune-free shadow zones behind positive relief obstacles. The presence of a depression found in the wind-shielded side of an obstacle could mean elevations low enough to interact with the underlying water table, as an increase in moisture could trap sediment, preventing the formation and migration of dunes. For example, the shadow zone of obstacles in Libya extends 44 m below the mean interdune elevation surface, which is within the range of the near surface Nubian Sandstone Aquifer System (Sefelnasr et al., 2015). In one instance, a lacustrine feature is formed within the shadow zone of an obstacle in Mali (Figure 6d) and in other instances evaporites are observed within the obstacle shadow zone (Figure 6c).

In negative relief obstacles, dunes occupy the leeward side of the obstacle, but formed at a spacing greater than that of the surrounding dune field (Table 2a). Although a number of factors affect dune wavelength, low sediment availability appears to play a strong role in creating the wider spaced dunes in the Kalahari. In this case, some sediment likely bypasses through the pans and is deposited downwind. Alternatively, various generations of dunes are recognized to have formed within the Kalahari over the past 20,000 years (Lancaster, 1989) and the wider spacing may reflect previous formative wind and sediment availability conditions.

5.4 Titan dune-topography interaction comparisons

By using the observed relationships on Earth between topography and dune morphology, interpretations can be made about the topographic obstacles observed on Titan. Many of Titan's obstacles appear to exhibit the strong dune deflection of a positive relief Earth obstacle (Fig. 8e, f and Fig.1a-1c), implying that the obstacles are both positive relief and have steep windward slopes. Several obstacles on Titan, however, show little or no deflection of dune crestlines (Figure 1d). This is consistent with the neutral topography on Earth. Notably, the up to 70-degree deflection of crestlines observable along the windward face negative topography on Earth (Figure 10) can be found for a few obstacles on Titan (Figure 16a, c). Although this could be interpreted to mean that negative topography exists on Titan, the steep slopes found along the windward side of the Earth negative topography may drive the deflection in negative topography as it does in positive topography and thus we cannot discriminate between positive and negative topography on Titan.

Despite the archetypical image of Titan's tear-dropped shaped obstacles, 92% of the obstacles we measured on Titan do not have a shadow zone void of dunes. This could imply a number of conditions about the dune fields on Titan. The absence of a shadow zone may imply that Titan's obstacles are more like the neutral topography measured in this study or do not have exceptionally high windward slopes that would affect the sediment transport. It could also imply that sediment supply is abundant and that winds are strongly bimodal, which would allow sand to enter the shadow zone from the sides. Lastly, the range of boundary conditions on Titan is different from Earth and

may variably promote or limit the formation of a dune-free shadow zone. For example, dune-free shadow zones could form where the dune-free zone is a depression and interacts with a shallow liquid table, which would be consistent with observations of sediment availability limited dune morphologies in Titan's dune fields (Ewing et al., 2015).

5.5 Sediment availability and wind direction

Identifying a resultant wind and sand transport direction is possible on Titan when considering the analysis done for the Earth analogs where we know wind conditions. It is clear based on the wind data and resultant sand flux roses that the dune-shadow zone is associated exclusively with the wind-shielded side of an obstacle (Figure 8b, d, e,f,). However, while the shadow zone indicates a net wind and sediment transport direction, it does not match those two parameters exactly in orientation (Figure 18a), and so can only be used as a broad indicator of wind and sediment transport direction. Furthermore, this obstacle shadow zone is characterized by either a dune free zone or a widening of crestlines between 1.05 and 1.67x the dune-field mean (Table 2b). For Titan, where only 8% of the obstacles studied have an identifiable dune-free shadow zone, the dune free regions are found only along the east-southeast obstacle sides in Fensal, and the east-northeast obstacle sides in Senkyo. Additionally, a widening of crestlines between 1.04 and 1.06x the dune-field mean is also associated solely with the east-southeast and east-northeast obstacle sides of Fensal and Senkyo, respectively (Table 2a).

Average dune wavelength along the windward side of the obstacles for the Earth analogs indicate another trend. While three of the five earth deserts show a decrease in dune wavelength on the windward side, between 62% and 93% of field mean, two of the five deserts show a slight increase in wavelength between 103% and 101%x (Table 2a) field mean. But, even when the windward side exhibits a slight increase in dune spacing, the accompanying wind-shielded side exhibits an even greater increase in dune spacing, so for one of the deserts with a slight dune spacing increase on the windward edge of 1.01x, the wind-shielded edge has an even greater dune spacing of 1.28x to the dune field mean. The other desert with a dune wavelength increase of 1.03x dune-field mean wavelength has a dune free shadow zone and so we cannot compare the two sides. Titan demonstrates the same trend, where there is a greater dune spacing along the east side, between 104% and 106% and a decrease in dune spacing along the west side, between 89% and 98%.

The distance away from an obstacle that reorientation of dunes occurs can be identified by the magnitude of the moving standard deviation (red) plotted on Figures 14, 15, and 16. For all of the Earth study areas, the moving standard deviation approaches to dune field mean 65% nearer the obstacle on the windward side when compared to the wind-shielded side. When applying these observations to the Titan west face and east face dune orientation plots (Figure 16a – d), we see that standard deviation returns to near dune field mean nearer the obstacle on the West side than the East side. This suggests the windward facing side is along the West and the wind-shielded side is along the east.

These analysis of the obstacle shadow zone, dune spacing, and deflection of crests relative to known wind and sediment transport directions for the Earth analogs would suggest a net sediment transport and wind direction from west to east across both Titan study areas, where more locally Fensal is more east-southeast and Senkyo is more east-northeast.

5.6 Interpreting wind and sand transport direction on Titan

Identifying a resultant wind and sand transport direction is possible on Titan when considering the analysis done for the Earth analogs where we know wind conditions. It is clear based on the wind data and resultant sand flux roses that the dune-shadow zone is associated exclusively with the wind-shielded side of an obstacle (Figure 8b, d, e,f,). However, while the shadow zone indicates a net wind and sediment transport direction, it does not match those two parameters exactly in orientation (Figure 18a), and so can only be used as a broad indicator of wind and sediment transport direction. Furthermore, this obstacle shadow zone is characterized by either a dune free zone or a widening of crestlines between 1.05 and 1.67x the dune-field mean (Table 2b). For Titan, where only 8% of the obstacles studied have an identifiable dune-free shadow zone, the dune free regions are found only along the east-southeast obstacle sides in Fensal, and the east-northeast obstacle sides in Senkyo. Additionally, a widening of crestlines between 1.04 and 1.06x the dune-field mean is also associated solely with the east-southeast and east-northeast obstacle sides of Fensal and Senkyo, respectively (Table 2a).

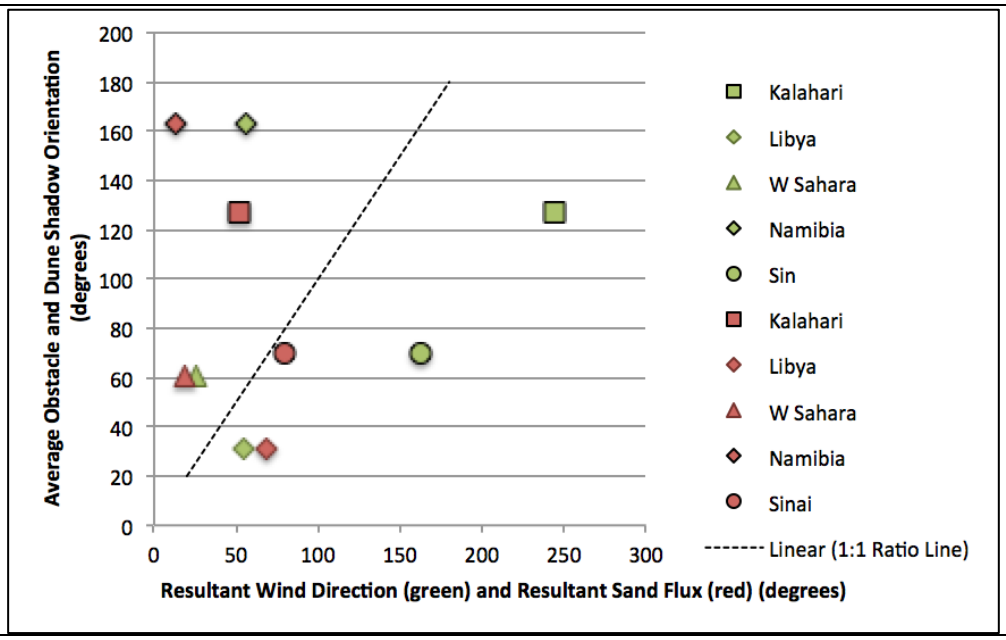

Figure 18a.

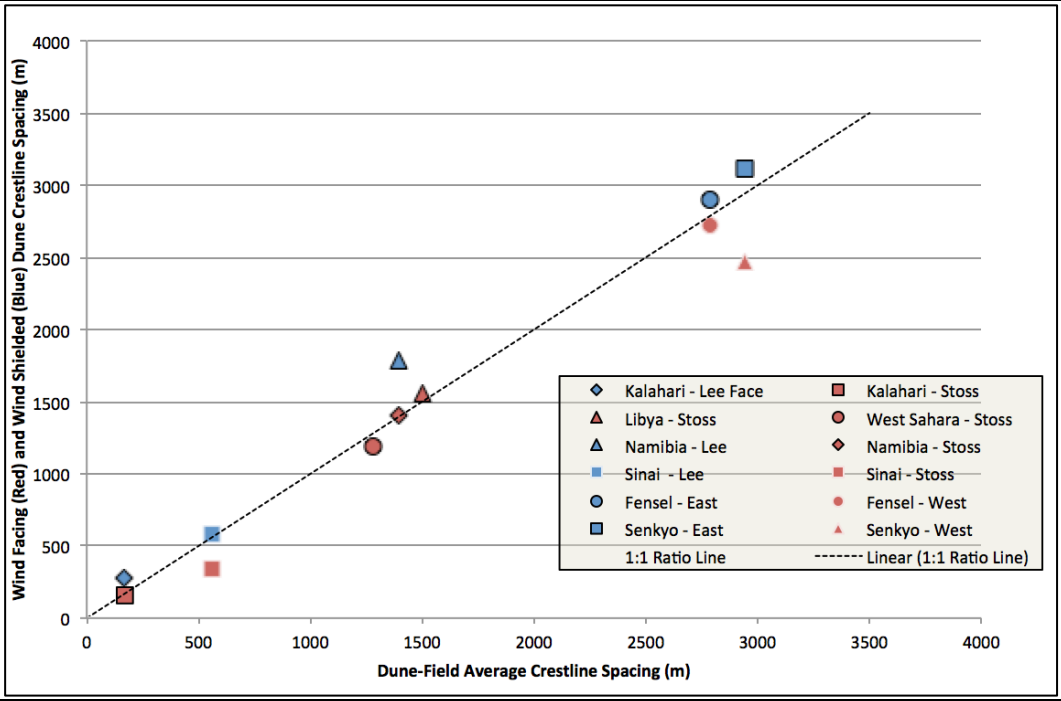

Figure 18b.

Figure 18. Plot of resultant wind direction and resultant sand flux against average obstacle dune shadow orientation for the Kalahari, Libya, West Sharaha, Namibia, and Sinai deserts (a). Plot of the stoss-ward and lee-ward crestline spacing against dune-field average crestline spacing for the Kalahari, Libya, Namibia, Sinai, West Sahara, Fensal, and Senkyo dune fields.

Average dune wavelength along the windward side of the obstacles for the Earth analogs indicate another trend. While three of the five earth deserts show a decrease in dune wavelength on the windward side, between 62% and 93% of field mean, two of the five deserts show a slight increase in wavelength between 103% and 101%x (Table 2a) field mean. But, even when the windward side exhibits a slight increase in dune spacing, the accompanying wind-shielded side exhibits an even greater increase in dune spacing, so for one of the deserts with a slight dune spacing increase on the windward edge of 1.01x, the wind-shielded edge has an even greater dune spacing of 1.28x to the dune field mean. The other desert with a dune wavelength increase of 1.03x dune-field mean wavelength has a dune free shadow zone and so we cannot compare the two sides. Titan demonstrates the same trend, where there is a greater dune spacing along the east side, between 104% and 106% and a decrease in dune spacing along the west side, between 89% and 98%.

The distance away from an obstacle that reorientation of dunes occurs can be identified by the magnitude of the moving standard deviation (red) plotted on Figures 14, 15, and 16. For all of the Earth study areas, the moving standard deviation approaches to dune field mean 65% nearer the obstacle on the windward side when compared to the wind-shielded side. When applying these observations to the Titan west face and east face dune orientation plots (Figure 16a – d), we see that standard deviation returns to near dune field mean nearer the obstacle on the West side than the East side. This suggests the windward facing side is along the West and the wind-shielded side is along the east.

These analysis of the obstacle shadow zone, dune spacing, and deflection of crests relative to known wind and sediment transport directions for the Earth analogs would suggest a net sediment transport and wind direction from west to east across both Titan study areas, where more locally Fensal is more east-southeast and Senkyo is more east-northeast.

6. CONCLUSIONS

The interaction between sand dune patterns and topographic obstacles is considered a primary signal of sand transport direction in the equatorial region of Saturn's moon, Titan. We find a robust connection between the spatial manifestation of topographic-obstacle morphology and dune pattern changes that provide a means to interpret dune-obstacle interaction on Titan. The primary conclusions from the analog study of Earth dune-obstacles are that obstacles types vary in type and morphology and may be positive, negative or neutral relief formed by bedrock or deflation of dune-field sediments. The degree of deflection of dunes around an obstacle recognized by the deviation of the dune orientation from the mean dune-field crestline orientation relates to the steepness of the windward slope of an obstacle. Dune-free zones adjacent to obstacles typically form on the leeward side of positive relief obstacles, but a number of boundary conditions, including surface moisture, play a role in determining the size and shape of the shadow zone. Where shadow zones do form, these zones align with the resultant wind and sand transport directions. These key relationships support the west to east sediment transport direction inferred on Titan based on dune-obstacle interactions. However, the range of dune-obstacle morphologies on Titan also reveal that Titan's obstacles may also form with the same range of diversity as on Earth and that boundary conditions on Titan, as on Earth, may play a significant role in determining the morphology of dune-interactions.

REFERENCES

Bagnold, Ralph A. 1942. *The Physics of Blown Sand and Desert Dunes*. 1st ed. New York, New York.

Benito, G A De. 1974. "Sand Dune Stabilization at El Aaiun - West Sahara." *Sixth International Biometeorological Congress* 18(2): 142–44.

Bristow, C. S., and S. J. Armitage. 2015. "Dune Ages in the Sand Deserts of the Southern Sahara and Sahel." *Quaternary International*: 1–12. http://dx.doi.org/10.1016/j.quaint.2015.07.062.

Callegari, Mattia et al. 2014. "Dune Height Estimation on Titan Exploiting Pairs of Synthetic Aperture Radar Images With Different Observation Angles." *IEEE Journal of Selected Topics in Applied Earth Observations and Remote Sensing*: 1–12.

Charman, J. H., and G. West. 2011. "Particle Size Distribution of Dune Sand from Libya." *Quarterly Journal of Engineering Geology and Hydrogeology* 44: 277–80. http://qjegh.lyellcollection.org/cgi/doi/10.1144/1470-9236/09-045.

Charnay, Benjamin., Barth, Erika., Rafkin, Scot., Narteau, Clement., Lebonnois, Sebastien., Rodriguez, Sebastien., Courrech du Pont, Sylvain., Lucas, Antoine. 2015. "Methane Storms as a Driver of Titan's Dune Orientation." *Nature Geoscience* 8(May): 362–66. http://www.nature.com/doifinder/10.1038/ngeo2406.

Elachi, C et al. 2006. "Titan Radar Mapper Observations from Cassini ' S T 3 Fly-By." *Nautre* 441(June): 709–14.

Ewing, Ryan C., Alex G. Hayes, and Antoine Lucas. 2014. "Sand Dune Patterns on Titan Controlled by Long-Term Climate Cycles." *Nature Geoscience* 8(January): 15–19. http://www.nature.com/doifinder/10.1038/ngeo2323.

Ewing, Ryan C., and Gary a. Kocurek. 2010. "Aeolian Dune Interactions and Dune-Field Pattern Formation: White Sands Dune Field, New Mexico." *Sedimentology* 57: 1199–1219.

Ewing, Ryan C., Gary Kocurek, and Larry W. Lake. 2006. "Pattern Analysis of Dune-Field Parameters." *Earth Surface Processes and Landforms* 31(March): 1176–91.

Fenton, Lori K., Timothy I. Michaels, and Ross a. Beyer. 2014. “Inverse Maximum Gross Bedform-Normal Transport 1: How to Determine a Dune-Constructing Wind Regime Using Only Imagery.” *Icarus* 230: 5–14. http://linkinghub.elsevier.com/retrieve/pii/S0019103513001619 (September 5, 2014).

Garzanti, Eduardo et al. 2012. “Petrology of the Namib Sand Sea: Long-Distance Transport and Compositional Variability in the Wind-Displaced Orange Delta.” *Earth-Science Reviews* 112(3-4): 173–89. http://dx.doi.org/10.1016/j.earscirev.2012.02.008.

Goldberg, David M., and J. Richard Gott. 2006. “Flexion and Skewness in Map Projections of the Earth.” *Princeton University Dept. of Physics* 2(1): 31. http://arxiv.org/abs/astro-ph/0608501.

Goudarzi, Gus H. 1970. “Geology and Mineral Resources of Libya. A Reconnaissance.” *US Geological Survey, Professional Paper*. http://www.scopus.com/inward/record.url?eid=2-s2.0-0014897005&partnerID=tZOtx3y1.

Guangqiang, Qian et al. 2012. “Airflow Patterns Upwind of Obstacles and Their Significance for Echo Dune Formation : A Field Measurement of the Effects of the Windward Slope Angle.” *Science China* 55(4): 545–53.

Hayward, Rosalyn K. et al. 2009. “Aeolian Dunes as Ground Truth for Atmospheric Modeling on Mars.” *Journal of Geophysical Research E: Planets* 114(11): 1–12.

Hueso, R., and a. Sánchez-Lavega. 2006. “Methane Storms on Saturn’s Moon Titan.” *Nature* 442(July): 428–31.

Jacobberger, P. A. 1988. “Mapping Abandoned River Channels in Mali Through Directional Filtering of Thematic Mapper Data.” *Remote Sensing of Environment* 26(2): 161–70.

Lancaster, N. 1981. “Grain Size Characteristics of Namib Desert Linear Dunes.” *Sedimentology* 28: 115–22. http://doi.wiley.com/10.1111/j.1365-3091.1981.tb01668.x.

Lancaster, N. 1986. “Grain-Size Characteristics of Linear Dunes in the Southwestern Kalahari.” *Journal of Sedimentary Petrology* 56(3): 395–400.

Lancaster, N. 1988. “Development of Linear Dunes in the Southwester Kalahari, Southern Africa.” *Journal of Arid Environments* 14: 233–44.

Lancaster, N. 1989. “Late Quaternary Palaeoenvironments in the Southwestern Kalahari 1.” *Palaeogeography, Palaeoclimatology, Palaeoecology* 70: 367–76.

Lancaster, N. and V.P. Tchakerian. 1996. “Geomorphology and Sediments of Sand Ramps in the Mojave Desert.” *Geomorphology* 17(1-3): 151–65.

Lancaster, N. et al. 2002. “Late Pleistocene and Holocene Dune Activity and Wind Regimes in the Western Sahara Desert of Mauritania.” *Geology* 30(11): 991–94.

Lancaster, N. 2006. “Linear Dunes on Titan.” *American Association for the Advancement of Science* 312(5774): 702–3.

Lebonnois, Sébastien, Jérémie Burgalat, Pascal Rannou, and Benjamin Charnay. 2012. “Titan Global Climate Model : A New 3-Dimensional Version of the IPSL Titan GCM.” *Icarus* 218: 707–22.

Li, Sen, Xun-cheng Xia, Hong-lang Xiao, and Gen-sheng Yang. 2000. “Characteristics, Origin and Evolution Ages of Aeolian Sand in the Sahelian Region of Mali.” *Chinese Geographical Science* 10(2): 159–67. http://link.springer.com/10.1007/s11769-000-0024-7.

Liléo, Sónia et al. 2013. “Long-Term Correction of Wind Measurements. State-of-the-Art, Guidelinies and Future Work.” *Elforsk Report 13:18* (13:18): 94.

Lisenbarth. 1991. “Sand Desert Forms in Libya; Remote Sensing Analysis.” *The Geology of Libya; Third Symposium on the Geology of Libya* 6: 2235–55.

Lora, Juan M, Jonathan I Lunine, and Joellen L Russell. 2015. “GCM Simulations of Titan’s Middle and Lower Atmosphere and Comparison to Observations.” *Icarus* 250: 516–28. http://dx.doi.org/10.1016/j.icarus.2014.12.030.

Lorenz, R.D et al. 2006. “The Sand Seas of Titan: Cassini RADAR Observations of Longitudinal Dunes.” *Science Mag* 312(May).

Lorenz, Ralph D., and Jani Radebaugh. 2009. “Global Pattern of Titan’s Dunes: Radar Survey from the Cassini Prime Mission.” *Geophysical Research Letters* 36(3). http://doi.wiley.com/10.1029/2008GL036850 (February 20, 2015).

Luo, Wanyin, Zhibao Dong, Guangqiang Qian, and Junfeng Lu. 2012. “Wind Tunnel Simulation of the Three-Dimensional Airflow Patterns Behind Cuboid Obstacles at Different Angles of Wind Incidence, and Their Significance for the Formation of Sand Shadows.” *Geomorphology* 139-140: 258–70.

Malaska, Michael J. et al. 2015. “Material Transport Map of Titan: The Fate of Dunes.” *Icarus*. http://dx.doi.org/10.1016/j.icarus.2015.09.029.

Mastrogiuseppe, M. et al. 2014. “Titan Dune Heights Retrieval by Using Cassini Radar Altimeter.” *Icarus* 230: 191–97. http://dx.doi.org/10.1016/j.icarus.2013.09.028.

Mey, Jürgen, Dirk Scherler, Gerold Zeilinger, and Manfred R Strecker. 2015. “Journal of Geophysical Research : Earth Surface.” *AGU Publications* 120: 1–20.

Miller, R. McG. 2014. “Evidence for the Evolution of the Kalahari Dunes from the Auob River, Southeastern Namibia.” *Transactions of the Royal Society of South Africa* 69(March 2015): 195–204. http://www.tandfonline.com/doi/abs/10.1080/0035919X.2014.955555.

Muhs, Daniel R. et al. 2013. “Origin of the Sinai-Negev Erg, Egypt and Israel: Mineralogical and Geochemical Evidence for the Importance of the Nile and Sea Level History.” *Quaternary Science Reviews* 69: 28–48. http://dx.doi.org/10.1016/j.quascirev.2013.02.022.

Neish, Catherine D., Ralph D. Lorenz, Randolph L. Kirk, and Lauren C. Wye. 2010. “Radarclinometry of the Sand Seas of Africa’s Namibia and Saturn's Moon Titan.” *Icarus* 208(1): 385–94. http://dx.doi.org/10.1016/j.icarus.2010.01.023.

Ntinas, G. K. et al. 2014. “Airflow Patterns around Obstacles with Arched and Pitched Roofs: Wind Tunnel Measurements and Direct Simulation.” *European Jthenal of Mechanics, B/Fluids* 43: 216–29. http://dx.doi.org/10.1016/j.euromechflu.2013.09.004.

Parteli, Eric J R et al. 2009. “Dune Formation under Bimodal Winds.” *Proceedings of the National Academy of Sciences of the United States of America* 106(52): 22085–89.

du Pont, Sylvain Courrech, Clement Narteau, and Xin Gao. 2014. “Two Modes for Dune Orientation.” *Geology* 42(9): 743–46.

Radebaugh, J. et al. 2008. “Dunes on Titan Observed by Cassini Radar.” *Icarus* 194(2): 690–703. http://linkinghub.elsevier.com/retrieve/pii/S001910350700512X (September 17, 2014).

Radebaugh, J. et al. 2010. “Linear Dunes on Titan and Earth: Initial Remote Sensing Comparisons.” *Geomorphology* 121(1-2): 122–32. http://linkinghub.elsevier.com/retrieve/pii/S0169555X09000804 (September 16, 2014).

Radebaugh, Jani. 2013. “Dunes on Saturn’s Moon Titan as Revealed by the Cassini Mission.” *Aeolian Research* 11: 23–41. http://dx.doi.org/10.1016/j.aeolia.2013.07.001.

Roskin, Joel et al. 2011. “Age, Origin and Climatic Controls on Vegetated Linear Dunes in the Northwestern Negev Desert (Israel).” *Quaternary Science Reviews* 30(13-14): 1649–74. http://dx.doi.org/10.1016/j.quascirev.2011.03.010.

Roskin, Joel, Itzhak Katra, and Dan G Blumberg. 2014. “Particle-Size Fractionation of Eolian Sand along the Sinai–Negev Erg of Egypt and Israel.” *Geological Society of America Bulletin* 126(1-2): 47–65. http://gsabulletin.gsapubs.org/content/126/1-2/47.abstract.

Rubin, D M, and R E Hunter. 1987. “Bedform Alignment in Directionally Varying Flows.” *Science (New York)* 237(4812): 276–78. http://www.ncbi.nlm.nih.gov/pubmed/17772055.

Rubin, David M., and Hiroshi Ikeda. 1990. “Flume Experiments on the Alignment of Transverse, Oblique, and Longitudinal Dunes in Directionally Varying Flows.” *Sedimentology* 37(37): 673–84.

Rubin, David M., Haim Tsoar, and Dan G. Blumberg. 2008. “A Second Look at Western Sinai Seif Dunes and Their Lateral Migration.” *Geomorphology* 93(3-4): 335–42.

Said, Rushdi, and M. G. Barakat. 1958. “Jurassic Microfossils from Gebel Maghara, Sinai, Egypt.” *Micropaleontology* 4(3): 231–72.

Sefelnasr, Ahmed, Wolfgang Gossel, and Peter Wycisk. 2015. “Groundwater Management Options in an Arid Environment: The Nubian Sandstone Aquifer System, Eastern Sahara.” *Journal of Arid Environments* 122: 46–58. http://dx.doi.org/10.1016/j.jaridenv.2015.06.009.

Soderblom, Laurence A et al. 2007. “Correlations between Cassini VIMS Spectra and RADAR SAR Images : Implications for Titan’s Surface Composition and the Character of the Huygens Probe Landing Site.” *Planetary and Space Science* 55: 2025–36.

Stone, a. E C. 2013. “Age and Dynamics of the Namib Sand Sea: A Review of Chronological Evidence and Possible Landscape Development Models.” *Journal of African Earth Sciences* 82: 70–87. http://dx.doi.org/10.1016/j.jafrearsci.2013.02.003.

Swezey, C. 2001. 167 Palaeogeography, Palaeoclimatology, Palaeoecology *Eolian Sediment Responses to Late Quaternary Climate Changes: Temporal and Spatial Patterns in the Sahara*.

Thomas, D S G, D J Nash, P A Shaw, and C Van Der Post. 1993. "Present Day Lunette Sediment Cycling at Witpan in the Arid Southwestern Kalahari Desert." *Catena* 20: 515–27.

Tokano, Tetsuya. 2008. "Dune-Forming Winds on Titan and the Influence of Topography." *Icarus* 194(1): 243–62. http://linkinghub.elsevier.com/retrieve/pii/S0019103507004988 (September 17, 2014).

Tokano, Tetsuya. 2010. "Relevance of Fast Westerlies at Equinox for the Eastward Elongation of Titan's Dunes." *Aeolian Research* 2(2-3): 113–27. http://linkinghub.elsevier.com/retrieve/pii/S1875963710000091 (September 17, 2014).

Tsoar, Haim. 1983. "Wind Tunnel Modeling of Echo and Climbing Dunes." *Developments in Sedimentology* 38(C): 247–59.

Tsoar, Haim. 1995. "Desertification in Northern Sinai in the Eighteenth Century." *Climatic Change* (29): 429–38.

Ward, J D. 1988. "Eolian, Fluvial, and Pan (Playa) Facies of the Tertiary Tsonab Sandstone Formation in the Central Namib Desert, Namibia." *Sedimentary Geology* 55: 143–62.

Wasson, R.J., and R. Hyde. 1983. "Factors Determining Desert Dune Type." *Nature* 304: 337–39.

Wilson, Ian. G. 1972. "Aeolian Bedforms-Their Development and Origins." *Sedimentology* 19: 173–210.

Xianwan, Liu, Li Sen, and Shen Jianyou. 1999. "Wind Tunnel Simulation Experiment of Mountain Dunes." *Journal of Arid Environments* 42: 49–59.

Xiao, JianHua et al. 2015. "Morphology and Formation Mechanism of Sand Shadow Dunes on the Qinghai-Tibet Plateau." *Journal of Arid Land* 7(1): 10–26. http://link.springer.com/10.1007/s40333-014-0074-9.

APPENDIX

WIND TUNNEL MODELING

To support and elaborate on the mapping and spatial characterization of dune topography interactions, a series of wind tunnel experiments were planned. Wind tunnel experiments examine the formation of linear ripples in the presence of obstacles of different shapes. The use of ripple morphology as a proxy for dune morphology is based on the idea that both dunes and ripples show a similar pattern–scale of bedform, which has similar fundamental processes (Pelletier, 2009; Ewing, 2006). As such, we could test a range of obstacle morphologies under a more controlled and uniform setting that that found in nature.

For the methodology we planned to vary obstacle height, length, and width ratios to test how ripples will respond to various types of topography observed for the Earth obstacles studied. A series of 40 to 50 images at a range of heights and locations around the wind tunnel platform ripples and obstacle were planned at timed intervals to import into a photogrammetric program. This would provide a way to digitize and quantitatively analyze how the ripples respond to varies obstacle morphologies placed in the wind tunnel.

Preliminary runs were conducted to demonstrate that linear dunes could be established in the wind tunnel. We started out experiments with a flat bed of mixed bimodal sediment size of 0.18 mm and 0.55 mm in a bed of around 2.5 cm in thickness. The bimodal size distribution was chosen so that the coarser grains would migrate to the

ripple crests, effectively highlighting ripple crest location. Rotating the wind tunnel platform 135 degrees every couple of minutes successfully resulted in linear ripples. Sediment was added incrementally outside the rotating platform to avoid surface armoring and my extension cessation of ripple migration. At this point an obstacle (wooden block in Figure 19a) was placed at the center of the rotating platform. The experiment was then repeated but this time a sloped obstacle made of green clay (Figure 19b) was placed at the center of the platform.

Preliminary results were encouraging for a couple of reasons: first we successfully produced linear ripples in the wind tunnel, and second we observed similar pattern-scale bedform morphology to what we observed for the Earth dune-obstacle interaction counterparts. For the preliminary run where we placed a wooden block in the center of the rotating platform, we observed ripple crest line deflection along the windward side of the block, scouring along the windward side of the block, and a lack of observed sediment transport along the wind-shielded side of the block (Figure 19a). For the clay obstacle preliminary run, we observed ripple crest line deflection on the windward side of the obstacle, scouring along the windward side of the obstacle, however not as much as observed with the wooden block, and a lack of observed sediment transport along the wind-shielded side of the block (Figure 19b).

Were we able continue to test a series of different obstacle morphologies and the resulting ripple patterns, we believe these experiments would help us better understand the relationships between obstacle morphology and dune patterns on both Earth and Titan. Due to the break down of the University of Texas at Austin wind tunnel, which

could not be repaired in time to conduct these experiments, we were not able to complete this portion of the study.

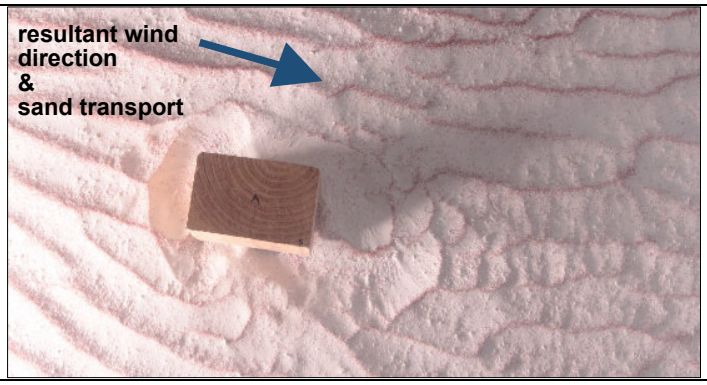

Figure 19a.

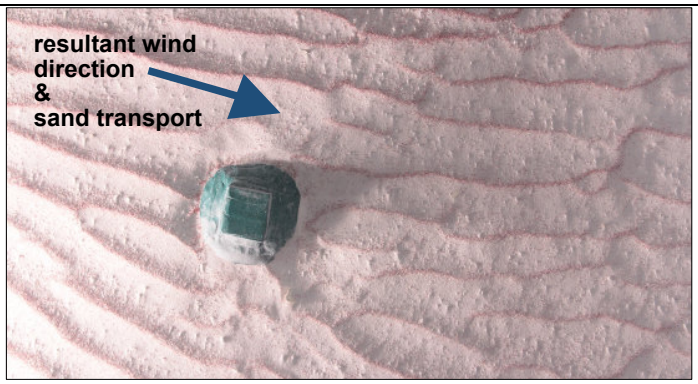

Figure 19b.

Figure 19. Image looking down on linear ripples formed in the wind tunnel with a wooden block (a), and a clay object (b) serving as a topographic-obstacle analog.

Planet	Desert Located Within	Obstacle ID	Location (Decimal Degrees)	Obstacle Width (km)	Obstacle Profile (km)	Obstacle Shadow Length (km)	Planimetric Area (km2)	Obstacle Relief Type	Normalized Obstacle Max Height (m)	Normalized Obstacle Min Height (m)
Earth	Sinai	S-A	33.465022 30.692274	22.060751	24.970251	16.995025	195.476	Positive	507	70
		S-B	33.523756 30.816781	15.042993	13.245879	16.617163	435.294	Positive	695	199
Earth	Western Sahara Desert	M-A	-9.474060 21.677336	7.234653	16.270249	15.650763	107.828	Neutral	51	-17
		M-B	-2.795118 17.387895	1.503691	1.894893	19923.116	2.7021	Positive	170	6
		M-C	-14.241795 21.328228	0.480919	4.256797	39.076931	4.083719135	Positive	182	66
Earth	Libyan Desert	L-A1	22.064978 24.953630	1.23133	0.719606	6.83825	0.996312637	Positive	139	6
		L-A2	22.056373 24.909945	5.626555	5.270549	6.626576	22.76580328	Positive	197	-17
		L-B1	22.020615 24.286094	9.142996	13.372905	17.662088	111.0132411	Neutral	122	-65
		L-B2	22.095885 24.230490	7.851853	10.142011	62.662006	64.04505349	Neutral	105	-31
		L-C1	20.888822 22.822856	3.602985	5.067118	3.027175	14.01526259	Positive	54	-25
		L-C2	20.948170 22.774912	8.833839	15.502218	14.945933	85.834289	Positive	121	-44
		L-D1	20.554042 22.570427	2.506512	2.404342	2.290227	6.030566363	Positive	176	76
		L-D2	20.605716 22.428770	33.294499	18.8597677	58.522653	357.9558669	Positive	244	-4
		L-D3	20.719075 22.305656	6.522101	7.23449	11.47767	31.18162674	Positive	249	102
		L-D4	20.598781 22.253525	6.132466	10.06094	20.644465	42.20977398	Positive	60	-9
		L-E	22.546206 25.222044	12.248558	14.3630498	3.027175	101.2696295	Neutral	100	-81
		L-F1	22.554209 20.183616	3.50752	4.76826	19.5821886	7.22554633	Neutral	61	9
		L-F2	22.550938 20.155625	0.387363	0.70469	4.5356	0.211958434	Neutral	66	30
		L-F3	22.540934 20.127457	2.86715	4.15866	22.184502	6.095263398	Neutral	91	27
		L-F4	22.527894 20.093319	5.45788	5.69434	16.44463	7.420975895	Neutral	118	30
Earth	Kalahari Desert	K-A	20.275654 -27.249793	4.921692	1.55216	24.259671	8.08623761	Negative	30	-34
		K-B1	20.380139 -27.162622	3.364912	3.351992	4.144093	7.99571391	Negative	19	-23
		K-B2	20.414988 -27.177570	2.35001	1.547242	3.678113	2.75016524	Negative	6	-50
		K-C	20.504037 -27.481732	5.587463	1.350172	4.908216	8.3355792	Negative	24	-20
		K-D	20.445629 -27.045191	2.688714	1.36274	4.62437	3.250117	Negative	29	-12
		K-E	20.535339 -26.999533	1.36798	0.74354	4.13628	0.740977335	Negative	-3	-35
		K-F	20.578707 -27.005843	1.217882	0.928535	4.357258	0.962806401	Negative	-7	-49
		K-G	20.504037 -27.481732	4.339822	2.55525	2.0224	6.95991588	Negative	14	-26
		K-H	20.706778 -27.492647	3.126433	3.51731	4.192351	8.8310735	Negative	17	-31
		K-I	20.882525 -27.430757	2.419502	2.419502	5.512924	5.59771329	Negative	-10	-31
		K-J	20.743753 -27.367974	10.524651	5.145	4.9061	3.59802328	Negative	5	-35
		K-K1	20.826793 -27.340464	2.670738	2.82449	3.680977	6.15590395	Negative	1	-35
		K-K2	20.893766 -27.373865	3.971086	2.416975	3.896035	1.81290931	Negative	1	-35
Earth	Namib Desert	N-A	15.263579 -25.372277	4.93947	7.386106	9.318733	24.1226361	Positive	229	-208
		N-B	15.424253 -25.805910	15.236524	8.273581	10.375526	70.623733	Positive	410	-161
		N-C	15.515868 -25.242295	4.46835	6.444119	3.016455	26.391203	Positive	302	-15
		N-D	15.524237 -25.242179	6.804458	6.871165	6.208432	63.3684346	Positive	729	97
Titan	Fensel Dune Field	Fen-A	-46.706949 8.653944	30.419039	130.863778	38.306627	3149.762572	?	?	?
		Fen-B	-42.408959 8.063924	22.075392	33.126394	42.3683177	644.2073816	?	?	?
		Fen-C1	-35.245869 2.277576	9.702101	21.277539	33.375838	157.8773319	?	?	?
		Fen-C2	-34.789139 2.347084	11.787241	23.048736	9.813218	186.5064214	?	?	?
		Fen-C3	-34.364089 2.577517	14.792773	14.8211133	12.550401	364.3293577	?	?	?
		Fen-D1	-39.379985 -6.342364	25.00158	21.08064	28.225396	320.9336775	?	?	?
		Fen-D2	-38.633277 -6.114115	24.099348	24.099348	25.092911	379.4587874	?	?	?
Titan	Senkyo Dune Field	Sen-A1	106.527579 -12.002871	15.177947	34.64974	4.042843	264.2450401	?	?	?
		Sen-A2	106.898699 -11.819191	10.575433	19.679831	9.2380462	138.621749	?	?	?
		Sen-A3	107.248612 -11.635510	19.846258	23.552561	6.775072	254.6502069	?	?	?
		Sen-B1	108.895188 -6.559673	2.47141	6.659289	3.735541	11.51010367	?	?	?
		Sen-B2	109.496048 -6.705675	10.705343	27.32448	14.720302	223.5855726	?	?	?
		Sen-C1	103.936686 -11.525776	2.84579	3.811822	6.284001	8.561565062	?	?	?
		Sen-C2	104.388215 -11.633512	10.257032	17.270025	13.429493	72.03055401	?	?	?
		Sen-C3	104.397935 -11.792466	1.541226	3.433306	5.610472	3.308418355	?	?	?
		Sen-D	97.180595 -6.951508	19.667308	47.151972	25.772916	471.9304202	?	?	?
		Sen-E	78.776495 7.524181	17.297688	56.0400166	8.99585	733.5072465	?	?	?
		Sen-F1	108.240878 -9.492828	7.580952	7.7000628	8.49148	56.8538524	?	?	?
		Sen-F2	108.935163 -9.411496	5.005485	9.602635	5.895718	34.51236831	?	?	?
		Sen-F3	108.586749 -8.956546	32.577184	50.787874	47.477366	1152.452368	?	?	?
		Sen-F4	110.489038 -9.518244	7.844844	9.096394	6.837818	49.11926496	?	?	?
		Sen-G1	108.098913 -10.316680	5.943525	4.64788	6.10222	21.38612442	?	?	?
		Sen-G2	108.514213 -10.178331	6.7733	19.415665	7.426169	92.81916355	?	?	?
		Sen-G3	108.982531 -10.552168	20.358444	49.92659	45.076566	630.2985465	?	?	?
		Sen-G4	109.821968 -10.254865	16.646366	57.902508	23.85046	691.8893906	?	?	?

Table 1. Physical parameters of all the obstacles studied. Obstacle IDs are assigned based on desert location, a alphabetic letter, and a numeric value if the obstacle is within one obstacle diameter of another obstacle, where both obstacles will then have the same letter but a different number.

Dune Spacing Relative to Topographic-Obstacle Side						
		Dune Field				
Ratio of Obstacle Face Dune Spacing to Average Unmodified Dune Field Dune Spacing	Obstacle Face	Kalahari	Libya	Western Sahara	Namibia	Sinai
	Side W1	0.80999131	0.98323914	0.8312615	0.58150332	0.50557759
	Side W2	0.6416168	0.90648727	0.52473751	0.53112114	0.36298463
	Side S1	1.16137154	0.88553219	0.72099695	0.94538191	N/A
	Side S2	1.10635925	0.936167	0.44475894	0.71103178	0.62538307
	Wind-Shielded Side	1.66507106	N/A	N/A	1.28326141	1.0490474
	Wind-Facing Side	0.93216364	1.03187364	0.93302004	1.01123059	0.61975555

Table 2a.

Dune Spacing Relative to Topographic-Obstacle Side			
		Dune Field	
Ratio of Obstacle Face Dune Spacing to Average Unmodified Dune Field Dune Spacing	Obstacle Face	Fensel	Senkyo
	Side East-1	0.91937701	0.9760408
	Side East-2	0.99840811	0.89517319
	Side West-1	0.83799029	0.76519506
	Side West-2	0.92387171	0.74529831
	East Side	1.0397908	1.06000662
	West Side	0.9780839	0.83908211

Table 2b.

Table 2. Ratio of obstacle face dune spacing to the dune-field average dune spacing recorded at all sides of each target obstacle, with dune spacing averaged across each Desert study area on Earth (a) and each dune field study area on Titan (b)